ATTEL PROJECT

PERFORMANCE-BASED APPROACHES FOR HIGH STRENGTH TUBULAR COLUMNS AND CONNECTIONS UNDER EARTHQUAKE AND FIRE LOADINGS

Deliverable 5 – Model calibration

D.5.1. : Definition of stability curves

D.5.2. : D5.2: simulation data relevant to the selected typologies of base-joints, of HSS-CHS columns and HSS-CFT columns and of HSS-concrete composite beam-to-column joints

D.5.3. : Report on parametric numerical analyses

Contributing Partners:

Stahlbau Pichler
University of Liège
Centro Sviluppo Materiali
University of Thessaly
University of Trento

Summary

D.5.1. Definition of stability curves

In this section, the stability curves and axial load - bending interaction diagrams for tubular beam-columns as proposed in four major design specifications are presented in detail. The specifications are the API RP2A LRFD, Eurocode 3 (EN 1993), the CIDECT guidelines No.3, and the AISC specifications for Hollow Structural Sections, Those specifications are evaluated using experimental and numerical results from the present research in subsequent sections.

D.5.1.A. Recommended practice for Planning, Designing and Constructing Fixed Offshore Platforms- Load and Resistance Factor design [3]

A.1. Axial Compression

The recommendations given in this section are applicable to stiffened and unstiffened cylinders having a thickness $t \geq 6$mm, diameter-to-thickness ratio $D/t < 300$ and having yield strengths less than 414 MPa (60 ksi).

1.1.1.1. A.1.1. Column Buckling

The nominal axial compressive strength for tubular members subjected to column buckling should be determined from the yield stress according to the following equations:

$$F_{cn} = \left[1.0\text{-}0.25\lambda^2\right] F_y \quad \text{for} \quad \lambda < \sqrt{2} \qquad \text{(A.1.1-a)}$$

$$F_{cn} = \frac{1}{\lambda^2} F_y \quad \text{for} \quad \lambda \geq \sqrt{2} \qquad \text{(A.1.1-b)}$$

where

λ= column slenderness parameter defined as follows:

$$\lambda = \frac{KL}{\pi r}\left[\frac{F_y}{E}\right]^{0.5} \qquad \text{(A.1.1-c)}$$

where

F_{cn}= nominal axial compressive strength, in stress units
E= Young's modulus o elasticity
K= effective length factor
L=embraced length
r= radius of gyration

A.1.2 Local Buckling

The possibility of local buckling of the tubular members should be examined calculating the elastic and inelastic local buckling stresses as follows:

a) Elastic Local Buckling

The nominal elastic local buckling strength should be determined from:

$$F_{xe} = 2C_x E\left(t/D\right) \qquad \text{(A.1.2-1)}$$

where

F_{xe} =nominal elastic local buckling strength, in stress value

C_x = critical elastic buckling coefficient

D= outside diameter
t= wall thickness
x= subscript for the member longitudinal axis

The theoretical value of C_x is 0.6. However, a reduced value of C_x =0.3 is recommended for use in the above equation to account the effect of initial imperfections.

b) Inelastic Buckling

The nominal inelastic local buckling strength should be determined from:

$$F_{xc}=F_y \quad \text{for} \quad \frac{D}{t}\le 60 \qquad \text{(A.1.2-2)}$$

$$F_{xc}=\left[1.64-0.23\left(D/t\right)^{1/4}\right]F_y \quad \text{for} \quad \frac{D}{t}>60 \qquad \text{(A.1.2-3)}$$

Where

F_{xc} = nominal inelastic local buckling strength, in stress units

In case that $F_{xc} < F_{y,}$ or $F_{xe} <F_y$ a cylindrical member in compression is possible to fail due to local buckling. In order to calculate global (column) buckling, the nominal yield strength (F_y) in Eqs (A.1.1-a) & (A.1.1-b) is replaced by the minimum value between the nominal inelastic local buckling strength (F_{xc}) and the nominal elastic local buckling strength (F_{xe}).

A.2. Bending

The nominal bending strength (in stress units) for tubular members should be determined from the following equations in terms of the yield stress F_y and the diameter-to-thickness ratio:

$$F_{bn}=\left(\frac{W_{pl}}{W_{el}}\right)F_y \qquad \text{(A.2-a)}$$

For $D/t \le 10340/F_y$ (F_y in MPa)

For $D/t \le 1500/F_y$ (F_y in ksi)

$$F_{bn}=\left[1.13-2.58\left(\frac{F_yD}{Et}\right)\right]\left(\frac{W_{pl}}{W_{el}}\right)F_y \qquad \text{(A.2-b)}$$

For $10340/F_y \le D/t \le 20680/F_y$ (F_y in MPa)

For $1500/F_y < D/t \le 3000/F_y$ (F_y in ksi)

$$F_{bn}=\left[0.94-0.76\left(\frac{F_yD}{Et}\right)\right]\left(\frac{W_{pl}}{W_{el}}\right)F_y \qquad \text{(A.2-c)}$$

For $20680/F_y \le D/t \le 300$ (F_y in MPa)

For $3000/F_y < D/t \le 300$ (F_y in ksi)

Where

F_{bn} nominal bending strength, in stress units

W_{el} elastic section modulus $W_{el}=\pi R_m^{\,2}t$

W_{pl} plastic section modulus $W_{pl}=4R_m^{\,2}t$

A.3 Combined Axial Compression and Bending

Cylindrical members under combined axial compressive and bending loads should be designed to satisfy the mimimum of the following conditions:

$$\frac{f_c}{F_{cn}}+\frac{1}{F_{bn}}\left(\frac{f_{by}}{1-\frac{f_c}{F_{ey}}}\right)\le 1.0 \qquad \text{(A.3-a)}$$

and

$$1-\cos\left[\frac{\pi}{2}\frac{f_c}{F_{xc}}\right]+\left(\frac{f_{by}}{F_{bn}}\right)\le 1.0 \qquad \text{(A.3-b)}$$

where

f_c , compressive stress due to factor loads ($f_c<\varphi_c F_{cn}$)

f_b, bending stress due to factor loads($f_b<\varphi_b F_{bn}$)

F_{cn}, nominal axial compressive strength calculated in Eqs A.1, in stress units

F_{bn} nominal bending strength calculated in Eqs A.2, in stress units

φ_c=1, the resistance factor for axial compressive strength

φ_b=1, the resistance factor for bending strength

C_{my} reduction factor corresponding to the member y axis defined equal to 1 from the table D.3-1

F_{ey} Euler buckling strength corresponding to the member y axis, in stress units

$$F_{ey}=\frac{F_y}{\lambda_y^2} \qquad \text{(A.3-c)}$$

λ_y column slenderness parameter defined by Equation (B.1.1.1-c) [(D.2.2-2c)], where the parameters K, L and r are chosen to correspond to the bending about the y direction.

D.5.1.B. Eurocode 3: Design of steel structures

In order to calculate the buckling stress of a tubular member, the classification of the tubular cross section should be determined in accordance to Table 1.

Table 1 Classification limits for tubular cross-sections

<table>
<tr><td colspan="7">Tubular sections
 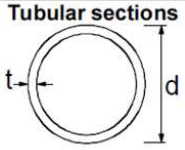
</td></tr>
<tr><td>Class</td><td colspan="6">Section in bending and/or compression</td></tr>
<tr><td>1</td><td colspan="6">$d/t \le 50\varepsilon^2$</td></tr>
<tr><td>2</td><td colspan="6">$d/t \le 70\varepsilon^2$</td></tr>
<tr><td>3</td><td colspan="6">$d/t \le 90\varepsilon^2$
NOTE For $d/t > 90\varepsilon^2$ see EN 1993-1-6.</td></tr>
<tr><td rowspan="3">$\varepsilon=\sqrt{235/f_y}$</td><td>$f_y$</td><td>235</td><td>275</td><td>355</td><td>420</td><td>460</td></tr>
<tr><td>ε</td><td>1,00</td><td>0,92</td><td>0,81</td><td>0,75</td><td>0,71</td></tr>
<tr><td>ε^2</td><td>1,00</td><td>0,85</td><td>0,66</td><td>0,56</td><td>0,51</td></tr>
</table>

B.1. Buckling strength in axial compression for tubular sections

When the tubular cross section is identified as class 1, 2 &3 then following procedure is followed according to EN-1993(part 1-1), otherwise, when class 4 is considered EN-1993-1-6 [EN-1993-1-6, 2007]should be followed:

B.1.1 Buckling strength in axial compression Class 1, 2 & 3 [EN-1993-1-1, 2005]

The buckling strength under axial compression for a tubular member is defined as follows

$$N_{b,Rd}=\chi A f_y \qquad \text{for class 1, 2 and 3} \qquad \text{(B.1.1-1)}$$

where

$N_{b,Rd}$: buckling strength under axial compression

χ : reduction factor for the corresponding buckling mode

A : area of the tubular cross section

For members subjected to axial compression, χ value is defined in terms of member slenderness as follows:

$$\chi = \frac{1}{\Phi+\sqrt{\Phi^2-\lambda^2}} \qquad \text{(B.1.1-2)}$$

where:

$$\Phi=0.5\left[1+\alpha\left(\lambda-0.2\right)+\lambda^2\right] \qquad \text{(B.1.1-3)}$$

and

$$\lambda=\sqrt{\frac{Af_y}{N_{cr}}}=\frac{L_{cr}}{i}\frac{1}{\lambda_1} \qquad \text{for class 1, 2 and 3} \qquad \text{(B.1.1-4)}$$

where

L_{cr}: the effective buckling length

i : radius of gyration

$$\lambda_1=\pi\sqrt{\frac{E}{f_y}}=93.9\varepsilon \qquad \text{(B.1.1-5)}$$

$$\varepsilon = \sqrt{\frac{235}{f_y}} \ (f_y \text{ in N/mm}^2) \qquad \text{(B.1.1-6)}$$

α : imperfection factor is defined in Table 2 (Section 6.1) based on the buckling curve Table 6.2(see EN-1993-1-1)

Table 2. Imperfection factors for stability curves

Buckling curve	**a0**	**a**	**b**	**c**	**D**
α	0.13	0.21	0.34	0.49	0.76

The buckling curve for hot-formed steel tubular members should be obtained from Table 6.2 (see EN-1993-1-1). For S235/ 275/ 355/ 420, "a" buckling curve is obtained and for S460 the "a_0".

When the tubular cross section is identified as class 4, the procedure below is followed according to EN-1993(part 1-6)[EN -1993-1-1, 2007]:

B.1.2 Buckling Strength Class4

In order to define the buckling curves for class 4 sections, we follow the procedure described below:

For class 4 cross sections the global relative member slenderness should be obtained from:

$$\lambda=\sqrt{\frac{N_{x,Rd}}{N_{Rcr}}} \qquad \text{(B.1.2-1)}$$

$N_{x,Rd}$ accounts for the critical meridional buckling load and N_{Rcr} accounts for the Eulerian elastic critical axial load which are given from Eq. B.1.2-2 and B.1.2-3, respectively:

$$N_{x,Rd}=\sigma_{x,Rd}A \quad \text{(B.1.2-2)}$$

The elastic meridional stress ($\sigma_{x,Rd}$) is defined according to the provisions of Annex D of EN-1993-1-6 as described in the following Sections (Section B.1.2.1) and the cross section area is denoted as A.

$$N_{Rcr} = \pi^2 \frac{EI}{(kL)^2} \quad \text{(B.1.2-3)}$$

where E is the elastic Young modulus, I is the inertia of the cross section and k is the effective buckling length factor based on the boundary conditions

In this case the buckling load (N_{Rd}) is defined as follows:

$$N_{Rd}=\chi(\lambda)\sigma_{x,Rd}A \quad \text{(B.1.2-4)}$$

where the factor $\chi(\lambda)$ is obtained from the combination of Eqs B.1.1-2, B1.1-3 and B.1.2-1

a. B.1.2.1 Local buckling stress design

(1)The buckling resistance should be represented by the buckling stresses as defined in 1.3.6. The design buckling stresses should be obtained from:

$$\sigma_{x,Rd}=\sigma_{x,Rk}/\gamma_{M1} \quad \text{(B.1.2.1-1)}$$

(2)The characteristic buckling stresses should be obtained by multiplying the characteristic yield strength by the buckling reduction factor χ:

$$\sigma_{x,Rk}=\chi_x f_{yk} \quad \text{(B.1.2.1-2)}$$

(3)The buckling reduction factor χ_x should be determined as a function of the relative slenderness of the shell λ from:

$$\chi=1 \quad \text{when} \quad \lambda_x \leq \lambda_0 \quad \text{(B.1.2.1-3a)}$$

$$\chi = 1-\beta\left(\frac{\lambda_x-\lambda_0}{\lambda_p-\lambda_0}\right)^{\eta} \quad \text{when} \quad \lambda_0 < \lambda_x < \lambda_p \quad \text{(B.1.2.1-3b)}$$

$$\chi = \frac{\alpha}{\lambda_x^2} \quad \text{when} \quad \lambda_p \leq \lambda_x \quad \text{(B.1.2.1-3c)}$$

where

α : elastic imperfection reduction factor
β : plastic range factor
η : interaction component
λ_0 : squash limit relative slenderness

The values of the above parameters (α, β, η, λ_0) should be taken from Annex D described below in section B.1.2.2
The value of the plastic limit relative slenderness λ_p should be obtained from:

$$\lambda_p=\sqrt{\frac{\alpha}{1-\beta}} \quad \text{(B.1.2.1-4)}$$

The relative shell slenderness parameter should be determined from:

$$\lambda_x=\sqrt{\frac{f_{yk}}{\sigma_{x,Rcr}}} \quad \text{(B.1.2.1-5)}$$

b. B.1.2.2 - ANNEX D

Expressions for buckling limit state evaluation using stress design are calculated as described below:

B.1.2.2.1 Elastic critical meridional buckling stress

(1)The following expressions may only be used for shells with boundary conditions BC1 or BC2 defined in Table 5.1 section 5 of EN-1993-1-6.
(2)The length of the shell segment is characterized in terms of the dimensionless length parameter ω:

$$\omega = \frac{l}{r}\sqrt{\frac{r}{t}} \qquad \text{(B.1.2.2-1)}$$

where

l: cylinder length between defined boundaries
r: radius of cylinder middle surface
t: thickness of shell

(3) The elastic critical meridional buckling stress ($\sigma_{x,Rcr}$), should be obtained from:

$$\sigma_{x,Rcr} = 0.605 E C_x \frac{t}{r} \qquad \text{(B.1.2.2-2)}$$

where C_x depends on the value of ω (see EN-1993-1-6, ANNEX D).

(3a) For medium-length cylinders, which are defined by:

$$1.7 \leq \omega \leq 0.5\ r/t \qquad \text{(B.1.2.2-3)}$$

The factor C_x should be taken as:

$$C_x = 1.0 \qquad \text{(B.1.2.2-4)}$$

(3b) For short cylinders, which are defined by:

$$\omega \leq 1.7 \qquad \text{(B.1.2.2-5)}$$

The factor C_x should be taken as:

$$C_x = 1.36 - \frac{1.83}{\omega} + \frac{2.07}{\omega^2} \qquad \text{(B.1.2.2-6)}$$

(3c) For long cylinders, which are defined by:

$$\omega > 0.5\ r/t \qquad \text{(B.1.2.2-7)}$$

The factor C_x should be taken as:

$$C_x = C_{x,N} \qquad \text{(B.1.2.2-8)}$$

In which $C_{x,N}$ is the greater of:

$$C_{x,N} = 1 + \frac{0.2}{C_{xb}}\left[1 - 2\omega\frac{t}{r}\right] \qquad \text{(B.1.2.2-9)}$$

And

$$C_{x,N} = 0.60 \qquad \text{(B.1.2.2-10)}$$

where C_{xb} is a parameter depending on the boundary conditions and being taken from table D.1

(3d) For long cylinders as defined in (3c) that satisfy the additional condition:

$$\frac{r}{t} \leq 150 \text{ and } \omega \leq 6\left(\frac{r}{t}\right) \text{ and } 500 \leq \frac{E}{f_{y,k}} \leq 1000 \qquad \text{(B.1.2.2-11)}$$

The factor C_x may alternatively be obtained from

$$C_x = C_{x,N}\left(\frac{\sigma_{xE,N}}{\sigma_{xE}}\right) + \left(\frac{\sigma_{xE,M}}{\sigma_{xE}}\right) \quad \text{(B.1.2.2-12)}$$

where
σ_{xE} is the design value of meridional stress $\sigma_{xE,d}$
$\sigma_{xE,N}$ is the component of $\sigma_{xE,d}$ that derives from axial compression (circumferentially uniform component)
$\sigma_{xE,M}$ is the component of $\sigma_{xE,d}$ that derives from tubular global bending (peak value of the circumferential varying component)

The following simpler expression may also be used in place of expression (B.1.2.2-12)

$$C_x = 0.6 + 0.4\left(\frac{\sigma_{xE,M}}{\sigma_{xE}}\right) \quad \text{(B.1.2.2-13)}$$

B.1.2.2.2 Meridional buckling parameters

(1) The meridional elastic imperfection reduction factor α_x should be obtained from:

$$\alpha = \frac{0.62}{1 + 1.91\left(\Delta w_k / t\right)^{1.44}} \quad \text{(B.1.2.2-14)}$$

where Δw_k is the characteristic imperfection amplitude:

$$\Delta w_k = \frac{1}{Q}\sqrt{\frac{r}{t}}t \quad \text{(B.1.2.2-15)}$$

(2) where Q is the meridional compression fabrication quality parameter which should be taken from the table D.2 (See EN-1993-1-6) for the specified fabrication tolerance quality class

(3)The meridional squash limit slenderness λ_0, the plastic range factor β, and the interaction exponent η should be taken as:

$\lambda_0 = 0.20$ $\beta = 0.60$ $\eta = 1.0$ (B.1.2.2-16)

(4) For long cylinders that satisfy the special conditions of B.1.2.2.11, the meridional squash limit slenderness λ_0 may be obtained from:

$$\lambda_0 = 0.20 + 0.10\left(\frac{\sigma_{xE,M}}{\sigma_{xE}}\right) \quad \text{(B.1.2.2-17)}$$

where
σ_{xE} is the design value of the meridional stress $\sigma_{xE,d}$
$\sigma_{xE,M}$ is the component of $\sigma_{xE,d}$ that comes from tubular global bending (peak value of the circumferential varying component)

(5) Cylinders need not be checked against meridional shell buckling if they satisfy:

$$\frac{r}{t} \le 0.03\frac{E}{f_{yk}} \quad \text{(B.1.2.2-18)}$$

B.2. Bending

The classification of the cross section should be defined from Table 5.2 of Eurocode 3 (EN-1993-1-1): Design of steel structures.

B.2.1 Bending Class 1, 2 & 3 [EN-1993-1-1, 2005]

(1)The tubular members under bending loads should be designed to satisfy:

$$\frac{M_{Ed}}{M_{c,Rd}} \leq 1.0 \qquad \text{(B.2.1-1)}$$

(2)The design value of bending moment is defined as follows:

$$M_{c,Rd}=M_{pl,Rd}=W_{pl}f_y \qquad \text{class 1 or 2} \qquad \text{(B.2.1-2a)}$$

$$M_{c,Rd}=M_{el,Rd}=W_{el,min}f_y \qquad \text{class 3} \qquad \text{(B.2.1-2b)}$$

where
W_{pl} is the plastic section modulus
W_{el} is the elastic section modulus

B.2.2 Bending Class 4 [EN-1993-1-6, 2007]

The design bending strength is defined as follows:

$$M_{x,Rd}=W_{el}\sigma_{x,Rd} \qquad \text{(B.2.2-1)}$$

where
$\sigma_{x,Rd}$ should be obtained from the equation (B.1.2.1-1) of EN1993-1-6 [7] and C_x may be obtained by equation (B.1.2-12) or (B.1.2-13), considering $\frac{\sigma_{xE,M}}{\sigma_{xE}}=1.0$ and $\frac{\sigma_{xE,N}}{\sigma_{xE}}=0$, for pure bending.

B.3 Combined loads

B.3.1 Class 1, 2 & 3 [EN-1993-1-1, 2005]

Classification of cross section is estimated in Table 5.1 (see EN-1993-1-1)
The stability of members with constant cross section not susceptible to torsional displacements (i.e. tubular members) should satisfy the following equations:

$$\frac{N_{Ed}}{\chi N_{Rd}}+k_{yy}\frac{M_{Ed}}{M_{Rd}} \leq 1.0 \qquad \text{(B.3.1-1)}$$

Where
N_{Ed}, $M_{y,Ed}$ are the design values of the axial compression and bending strength
χ reduction factor due to flexural buckling
k_{yy} interaction factor obtained from Annex A(Method1, see EN-1993-1-1)

For the interaction equation [B.3.1-1] simply supported members are considered with or without lateral supports subjected to axial compression and bending moments or lateral loads.

B.3.2 Class 4 [EN-1993-1-6, 2007]

The methodology proposed is described and the interaction curve is defined similar to section B.3.1, Eq (3.1-1):

$$\frac{N_{Ed}}{N_{Rd}}+k_{yy}\frac{M_{Ed}}{M_{x,Rd}} \leq 1.0 \qquad \text{(B.2.3.2-1)}$$

where
N_{Rd} is the axial load calculated in Eq. B.1.2-4 considering pure compression for class 4 cross sections according to EN-1993-1-6
$M_{x,Rd}$ is the moment strength calculated in Eq B.2.2-1 considering pure bending for class 4 cross sections according to EN-1993-1-6
k_{yy} is the interaction factor obtained from Annex A(Method1, see EN-1993-1-1)

D.5.1.C. Structural stability of hollow sections [6]

The classification of the tubular cross sections is defined from Table 4 (page 14) similar to EN1993-1-1 [9].

C.1 Tubular Members in axial compression for class 1, 2 & 3

The design buckling load of a compression member is given by the condition:

$$N_d \leq N_{b,Rd} \qquad \text{(C.1-1)}$$

Where

N_d is the working load and $N_{b,Rd}$ is the design buckling resistance capacity of the member

$$N_{b,Rd} = \chi A f_y \qquad \text{for class 1, 2 and 3} \qquad \text{(C.1-2)}$$

where χ accounts for the reduction factor of the relative buckling curve (Figure 3, Tables 11 -14) depending on the non-dimensional slenderness value (λ) of a column.

The buckling curves can be defined analytically by the equations (B.1.1-1&2) as described in EN-1993-1-1. Similarly, the member slenderness is calculated by Eq (B.1.1-4). The buckling curve for hot-formed high strength steel should be obtained from Table 10b (see [6]) or Table 6.2 (see EN1993-1-1 [9]).

It is noted that for grades S235/ 275/ 355/ 420, buckling curve "a" should be considered, while "a_0" curve corresponds to grades greater than S460.

C.2 Tubular members in bending for class 1, 2 &3

The design value of bending moment is defined similar to EN-1993-1-1 provisions described in B.2.1:

C.3 Members in combined compression and bending class 1, 2 & 3

The relation of compression and bending strength is based on the following linear interaction formulae:

$$\frac{N_{Sd}}{N_{b,Rd}} + K_y \frac{M_{Sd}}{M_{Rd}} \leq 1 \qquad \text{(C.3-1)}$$

Where

N_{sd} is the design value of axial compression

$N_{b,Rd}$ is the buckling load and is defined as follows:

$$N_{b,Rd} = \chi N_{pl} = \chi A f_y \qquad \text{(C.3-2)}$$

χ is the buckling reduction factor defined in section B.1, and f_y accounts for the yield strength

M_{sd} is the maximum absolute design value of the bending moment about y-y axis according to the first order theory.

M_{Rd} is the bending cross sectional strength defined as described previously in Section B.2.1

$$K_y = 1 - \frac{N_{Sd}}{\chi N_{pl}} \mu_y, \qquad \text{however } K_y \leq 1.5 \qquad \text{(C.3-3)}$$

$$\mu_y = \lambda_y \left(2\beta_{M,y} - 4\right) + \left(\frac{W_{pl}}{W_{el}} - 1\right), \quad \text{however } \mu_y < 0.9 \qquad \text{(C.3-4)}$$

where

$\beta_{M,y}$ is the equivalent uniform moment factors according to Table 16, column2(see [6]), in order to determine the form of the bending moment distribution M_y.

D.5.1.D. *AISC-Load and Resistance Factor Design Specification for Steel Hollow Structural Sections* [2]

D.1. Design Requirements

D.1.1. Classification of Steel Sections

HSS are classified for local buckling of the wall in compression as compact, noncompact,or slender-element cross-sections according to the limiting wall slenderness ratios λ_p and λ_r in Table 2.2-1 (see [2]). For an HSS to qualify as compact, the wall slenderness ratio λ must be less than or equal to λ_p. If λ exceeds λ_p but is less than or equal to λ_r, the HSS is noncompact. If λ exceeds λ_r, the HSS is a slender-element cross-section. The wall slenderness ratio λ shall be calculated as follows:

(a) For round HSS, $\lambda = D/t$, where D is the outside diameter and t is the wall thickness. This Specification is applicable only to round HSS with λ less than or equal to $0.448E/F_y$, where E is the modulus of elasticity and F_y is the specified minimum yield stress.

D.1.2 Design by Plastic Analysis

Design by plastic analysis is permitted when λ is less than or equal to λ_p for plastic analysis in Table 3, where $\lambda=D/t$.

Table 3. Limiting wall slenderness for compression elements

Element	Wall Slenderness Ratio, λ	Limiting Wall Slenderness	
		λ_p (compact)	λ_r (noncompact)
Round HSS	D/t [a]		
for axial compression		n.a.	$0.114E/F_y$
for flexure		$0.0714E/F_y$	$0.309E/F_y$
for plastic analysis		$0.0448E/F_y$	n.a.

[a] D/t must be less than or equal to $0.448E/F_y$

D.2 Tubular Compression Members

The design strength for flexural buckling of compression members is P_n:

$$P_n = F_{cr} A_g \qquad \text{(D.2-1)}$$

F_{cr} shall be determined as follows:

a) For $\lambda_c\sqrt{Q} \le 1.5$

$$F_{cr} = Q\left(0.658^{Q\lambda_c^2}\right)F_y \qquad \text{(D.2-2)}$$

b) For $\lambda_c\sqrt{Q} > 1.5$

$$F_{cr} = \left(\frac{0.877}{\lambda_c^2}\right)F_y \qquad \text{(D.2-3)}$$

where

$$\lambda_c = \frac{Kl}{r\pi}\sqrt{\frac{F_y}{E}} \qquad \text{(D.2-4)}$$

Q shall be determined as follows:

(a) For $\lambda \le \lambda_r$ in Section D.1.1, $Q = 1$

(b) For $\lambda > \lambda_r$ in Section D.1.1,

For round HSS with $\lambda < 0.448E/F_y$,

$$Q = \frac{0.0379E}{F_y\left(D/t\right)} + \frac{2}{3} \qquad \text{(D.2-5)}$$

D.3. Beams and other Flexural Members

For round HSS, for $\lambda \leq \lambda p$ in Section D.1.1, the cross sectional flexural capacity is given by:

$M_n = M_p = F_y Z$ (D.3-1)

(i) For $\lambda_p < \lambda \leq \lambda_r$,

$$M_n = \left(\frac{0.0207}{D/t} \frac{E}{F_y} + 1 \right) F_y S \quad \text{(D.3-2a)}$$

(ii) For $\lambda_r < \lambda \leq 0.448E/F_y$,

$$M_n = \frac{0.330E}{D/t} S \quad \text{(D.3-2b)}$$

where
S is the elastic section modulus
Z is the plastic section modulus

D.4 Members under Combined Forces

The interaction of flexure and axial force shall be limited by Eqs. (D.4-1a) and (D.4.1b)

(a) For $P_u/\varphi_c P_n \geq 0.2$,

$$\frac{P_u}{\varphi_c P_n} + \frac{8}{9} \left(\frac{M_{ux}}{\varphi_b M_{nx}} \right) \leq 1.0 \quad \text{(D.4-1a)}$$

(b) For $P_u/\varphi_c P_n < 0.2$,

$$\frac{P_u}{2\varphi_c P_n} + \left(\frac{M_{ux}}{\varphi_b M_{nx}} \right) \leq 1.0 \quad \text{(D.4-1b)}$$

P_u = required axial compressive strength, kips (N)
P_n = nominal compressive strength determined in accordance with Sections D.2 kips (N)
M_u = required flexural strength determined in accordance with LRFD Specification Section C1 [API-LRFD, 2000] described below, kip-in. (N-mm)
M_n = nominal flexural strength determined in accordance with Section D.3, kip-in.(N-mm)
x = subscript relating symbol to strong-axis bending
φ = 1 for compression
φ_b =1 for bending

D.5.2. Simulation data

The deliverable 5.2 deals the data simulation of: i) column elements at the section D.5.2.1; ii) column-base and beam-to-column joints at the section D.5.2.2

D.5.2.1. Simulation Data of HSS Columns

Aim of this section is the finite element simulation of CHS members' behaviour when subjected to various combinations of axial compressive load (N) and bending moment (M). The full scale tests performed on section A and B columns (task 3.3) were used to validate the finite element (FE) models developed by means of a commercial software. Such models have been then employed to define and extend the M-N interaction diagrams in the load regions not covered by experimental activity.

D.5.2.1.1. Model description

The finite element models have been developed adopting the commercial software MSC.MARC® which is able to deal with large strain, large displacement, material nonlinearities and instability phenomena typically involved in buckling of CHS members subjected to axial and bending loading.

Bilinear 4 noded shell elements with 7 integration points trough thickness were employed in order to properly simulate the local buckling phenomenon occurring both in bending than in axial load testing. This type of element is particularly suitable to describe curved surfaces subjected to large strains into plastic range. Solid element could also be employed for this purpose, but shell elements were preferred due to their lower consumption of computational resource, without affecting the results. An overview of the model employed for the simulations of tests on short specimens is reported in the Figure 1. Loads have been introduced in the model at end nodes (connecting the testing machine beams frame) by application of axial forces followed by an increasing rotation up to post buckling regime. An equivalent model has been employed to simulate the tests performed on long specimen.
A dedicated sensitivity analysis on mesh size in order to obtain the optimal balance in terms of accuracy and computation resource requirements was performed before the simulation of full scale tests. It was thus decided to employ 120 elements along circumference with an axial length of 10mm.

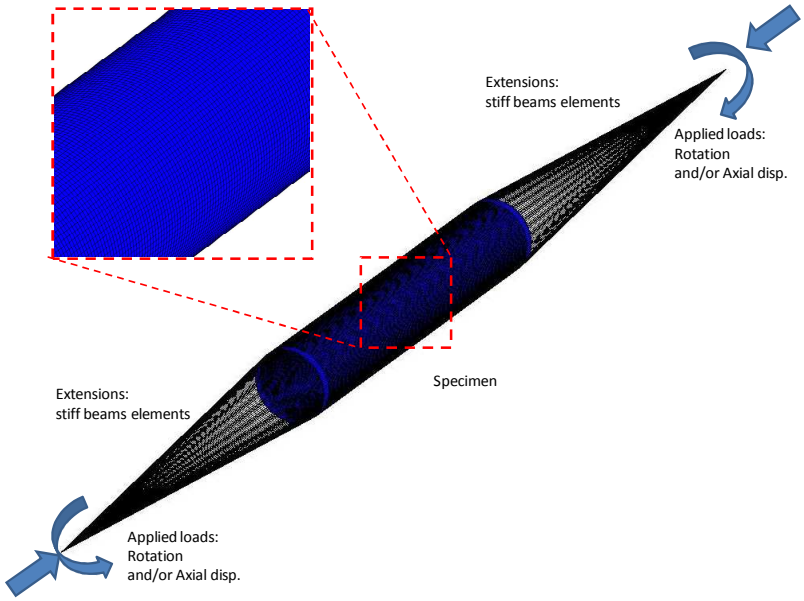

Figure 1. Overview of the FE model employed in the simulation of short column specimens

Material work hardening behaviour in terms of true stress – true stain curves, are needed as input to the model. Steel material has been characterized via tensile tests on cylindrical samples in longitudinal direction (task 3.1). The resultant curve used in finite element analysis (FEA) is reported in Figure 2. An isotropic hardening rule in combination with the Von Mises yield criterion has been adopted to describe the elastic-plastic behaviour of the CHS member deformation process.

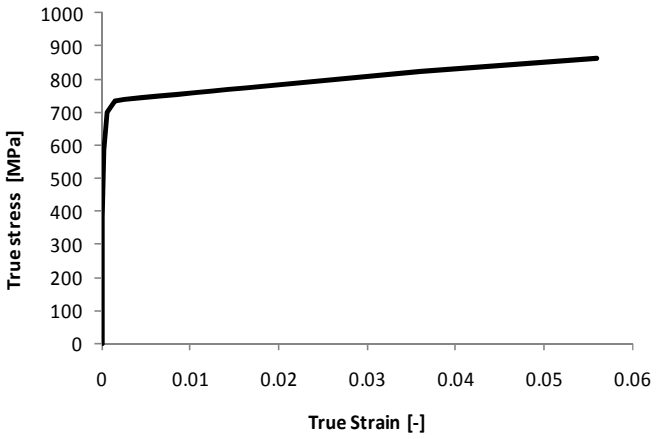

Figure 2**.** True stress true strain curve adopted in the FE model

Geometrical imperfections are introduced following the measured geometrical survey described in task 3.3.

D.5.2.1.2. Finite element model Main Results

Typical deformed shape and the equivalent plastic strain distribution is reported in the following Figure 3for a short specimen combined load test simulation. The plastic strain developed at compression side is influenced by the member imperfections and, as a result, buckling is driven in a position which is slightly away from the central section.

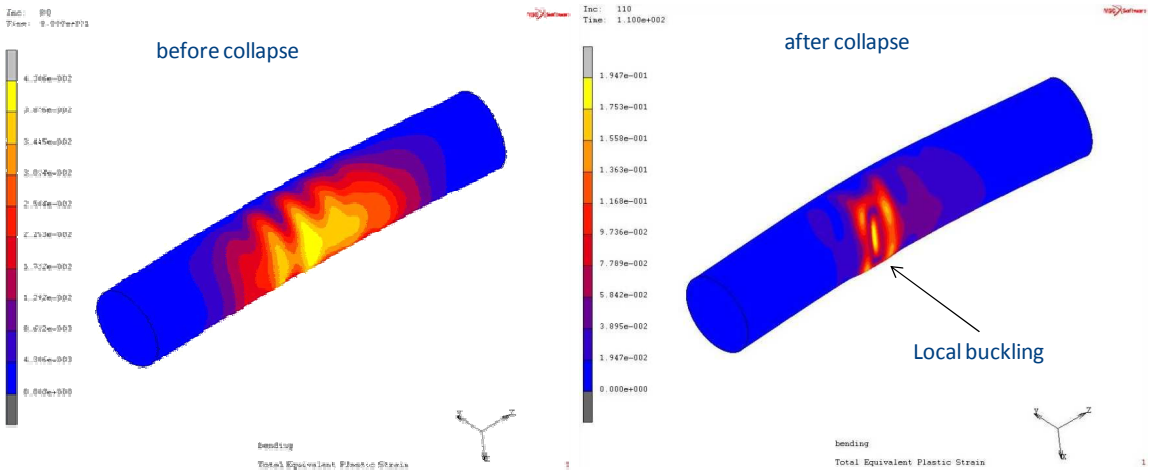

Figure 3. Deformed shape and plastic strain distribution during bending process

It is interesting to notice that the maximum value of the bending moment and the corresponding rotation angle are not significantly influenced by columns imperfections like those measured on the tested products. This is shown in Figure 4 by comparing a perfect model (constant thickness, perfect cylinder) with one where measured imperfections are introduced (thickness variation, dimples and ovality).
The measured residual stresses were found of negligible magnitude too (10% of yield stress) so they were not introduced in the model.

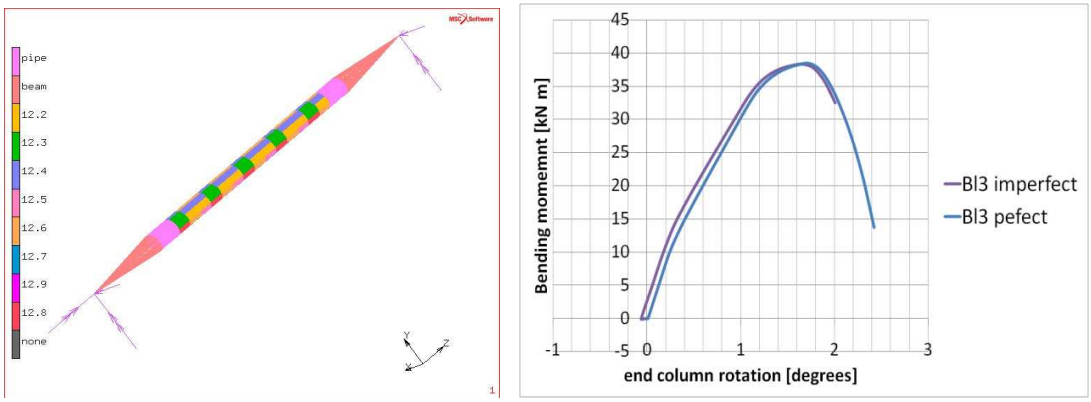

Figure 4. Geometrical imperfections: thickness variations introduced in the model (left) and comparison of moment vs. rotation diagrams obtained for geometrically "perfect" and "imperfect" models of long specimens (right).

The numerical results generally show very good agreement with the experimental combined load tests: a comparison between the experimental and numerical analysis results is reported in Figure 5 where moment vs. rotation curves for the As3-50 combined load configuration are reported. Both bending moment and rotation at limit point are very well predicted by FEA.

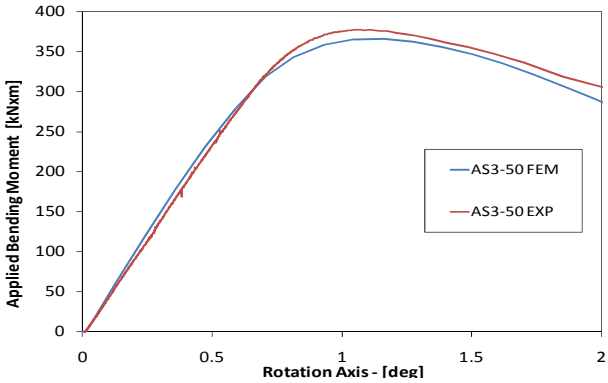

Figure 5. Comparison of experimental and numerical analysis results for the As3-50 combined load test

The performed analysis resulted in the definition of M-N interaction diagrams for short and long A and B specimens. Those are graphically reported in Figure 6 and Figure 7and in Table 4 and Table 5 where both experimental and numerical results are reported.

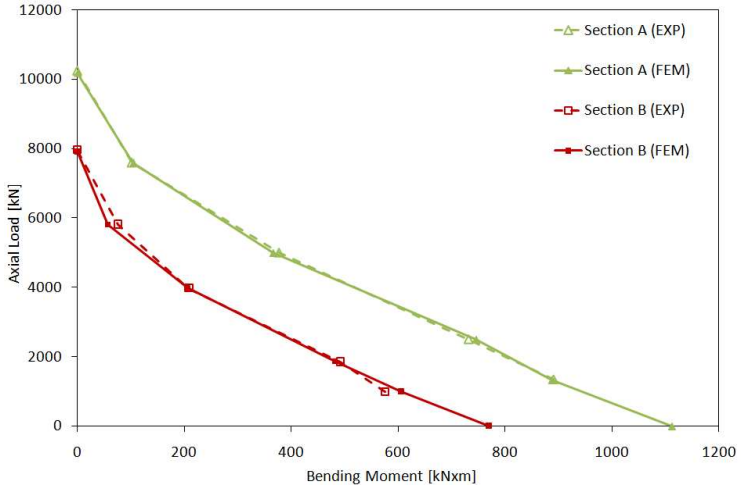

Figure 6. Experimental and numerical interaction diagram for short specimens of section A and B

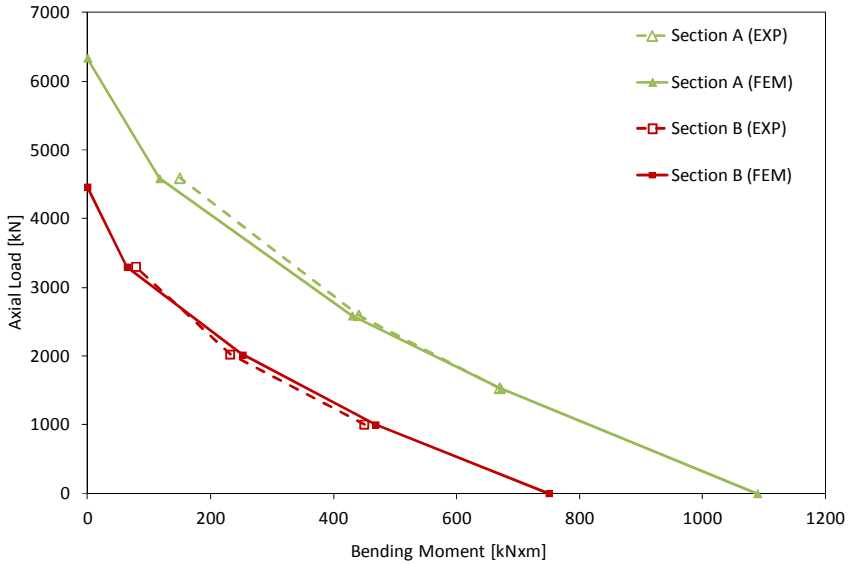

Figure 7. Experimental and numerical interaction diagram for long specimens of section A and B

Table 4. Summary of Experimental and numerical results for tests performed on long specimens

Case Id	Axial load kN		Moment kN m		Limit angle deg	
	Experim.	FEA	Experim.	FEA	Experim.	FEA
As3	-	0	-	1112	-	6
As3-13	1340	1340	891	888	2.6	2.3
As3-25	2500	2500	732	746	1.92	1.9
As3-50	5000	5000	377	366	1.1	1.2
As3-75	7600	7600	102	104	0.42	0.48
As1	10254	10194	-	-	-	-
Bs3	-	0	-	770	-	6
Bs3-13	1000	1000	575	606	2.4	2.4
Bs3-25	1865	1865	492	482	1.81	2.1
Bs3-50	3980	3980	209	206	0.98	1.1
Bs3-75	5822	5822	76	57	0.45	0.47
Bs1	7964	7934	-	0	-	0

Table 5. Summary of Experimental and numerical results for tests performed on long specimens

Case Id	Axial load kN		Moment kN m		Limit angle deg	
	Experim.	FEA	Experim.	FEA	Experim.	FEA
Al3_25	1530	1530	670	672	4.4	4.2
Al3_50	2590	2590	441	430	3.3	3.2
Al3_75	4588	4588	150	117	1.7	1.8
Bl3_25	1000	1000	450	468	4.2	4.5
Bl3_50	2020	2020	232	252	3.0	3.2
Bl3_75	3298	3298	79	64	1.5	1.9

D.5.2.1.3. Conclusions

Numerical analysis of the full scale tests by means of dedicated FE model developed in the commercial software MSC.MARC® have been performed.
Results show general good accordance with experimental results in terms of bending moment and rotation angle at buckling.
By means of the validated FE model, interaction M-N diagrams have been traced for sections A and B columns, extending the results of the experimental activity.
Actual geometrical imperfections measured in task 3.3 have been introduced for the simulation. Results show that the imperfections influence the plastic strain distribution during loading process but their very small magnitude has a negligible effect on the performance of the CHS members in terms of load carrying and rotational capacity up to failure.

D.5.2.2. Numerical analysis for columns in fire condition

This section presents the numerical analysis for the columns that were tested in fire within WP4, three HSS columns (C1, C2 and C3) and one composite column (C4). The geometries and materials of the columns can be found in Deliverable 4. The thermal characteristics of the materials are presented in Appendix A. SAFIR - a finite element code, developed in University of Liege, is used as the numerical tool.

Loading

As the both values and directions of the initial deflection of the columns are unknowns, in this numerical simulation, three cases of load are considered, as the show on Figure 8

Figure 8. Noting that an eccentricity e=10 mm is used in the tests (see Deliverable D4).

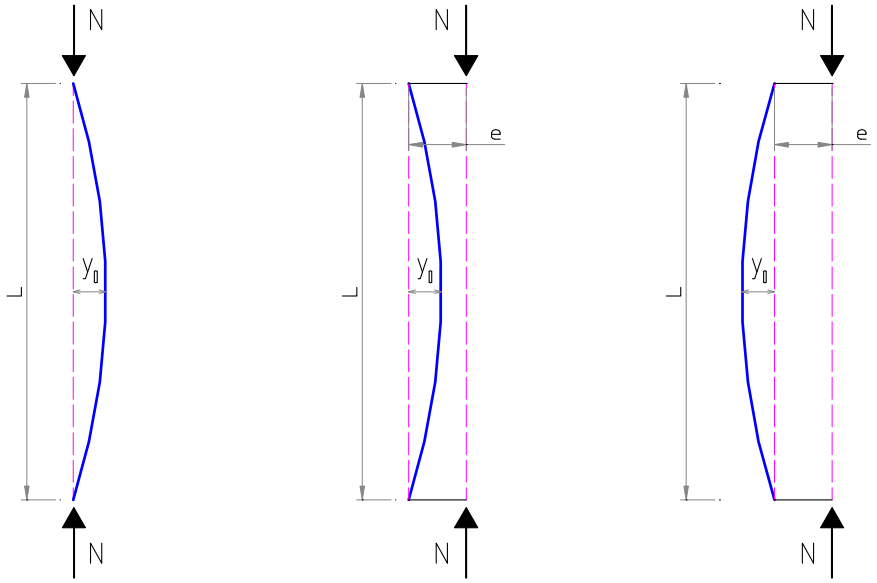

a) b) c)

Figure 8. Loading cases

FE modeling

Both beam and shell elements are used, Table 6 and Figure 9 to Figure 13 summarize the FE modelling of the columns.

Table 6. Adopted FE models for the columns

Thermal analysis→ Structural analysis ↓	2D solid element (Figure 9, Figure 10, and Figure 11)
Beam element (Figure 12)	Column C1, C2, C3, and C4
Shell element (Figure 13)	Column C1, C2, and C3

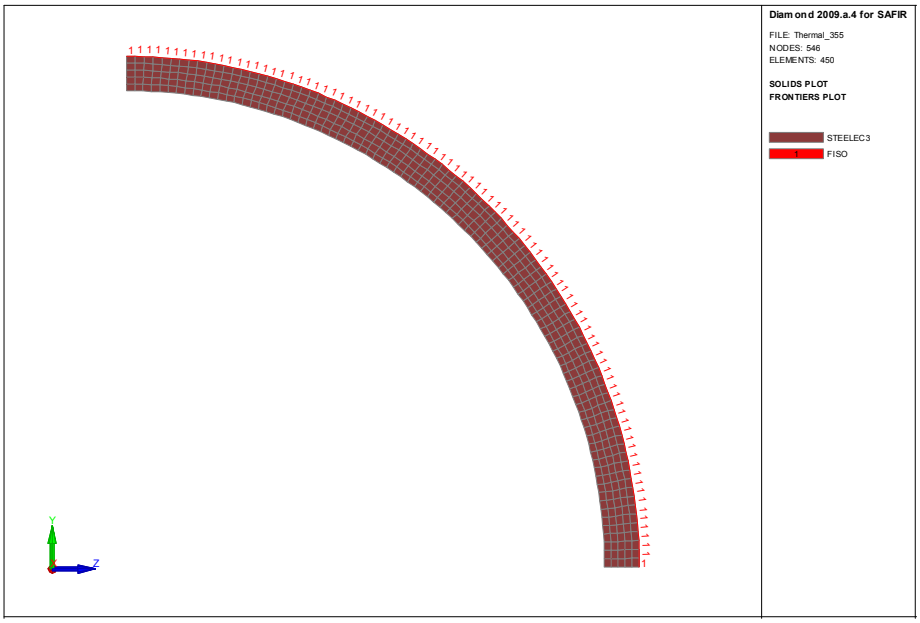

Figure 9. Columns C1, C2 and C3 – transversal discretization (for using beam element)

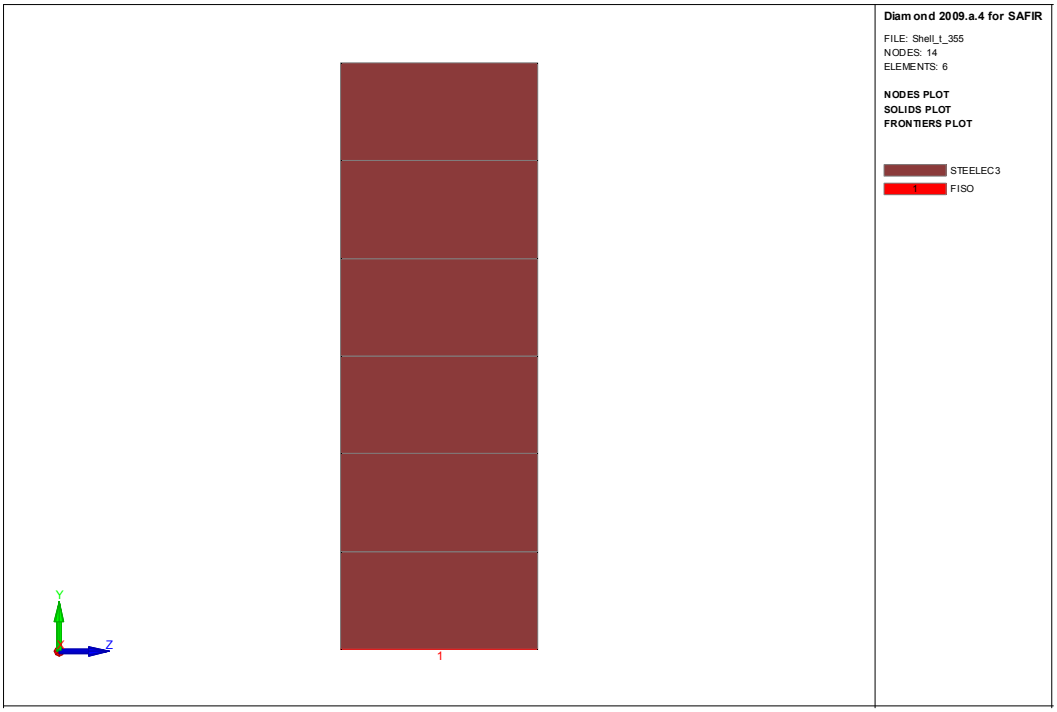

Figure 10. Columns C1, C2 and C3 – thickness discretization (for using shell element)

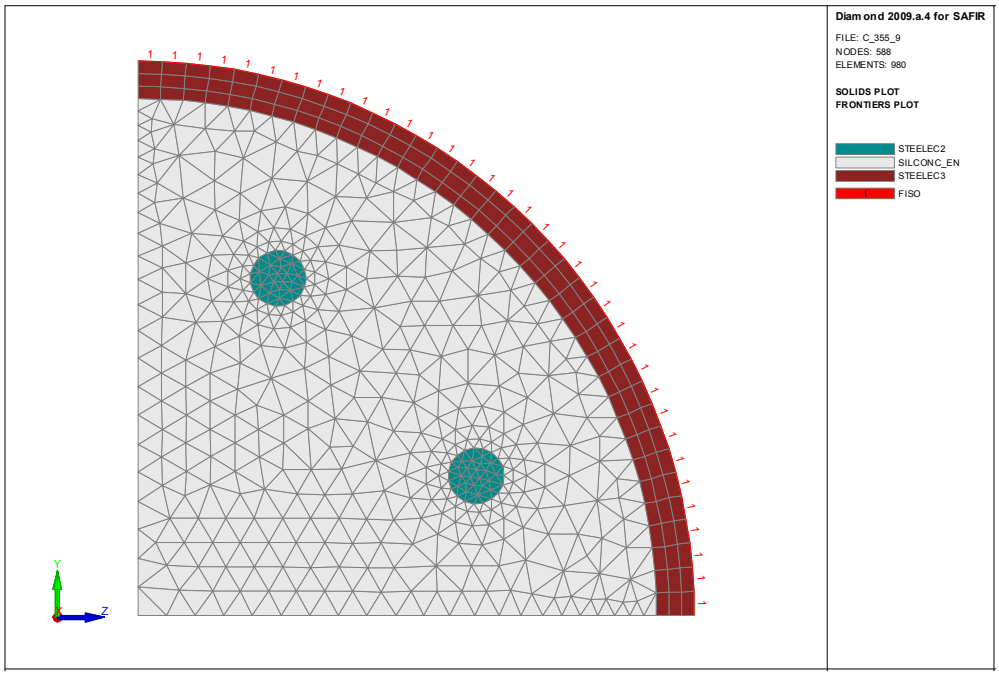

Figure 11. Column C4 – transversal discretization (for using beam element)

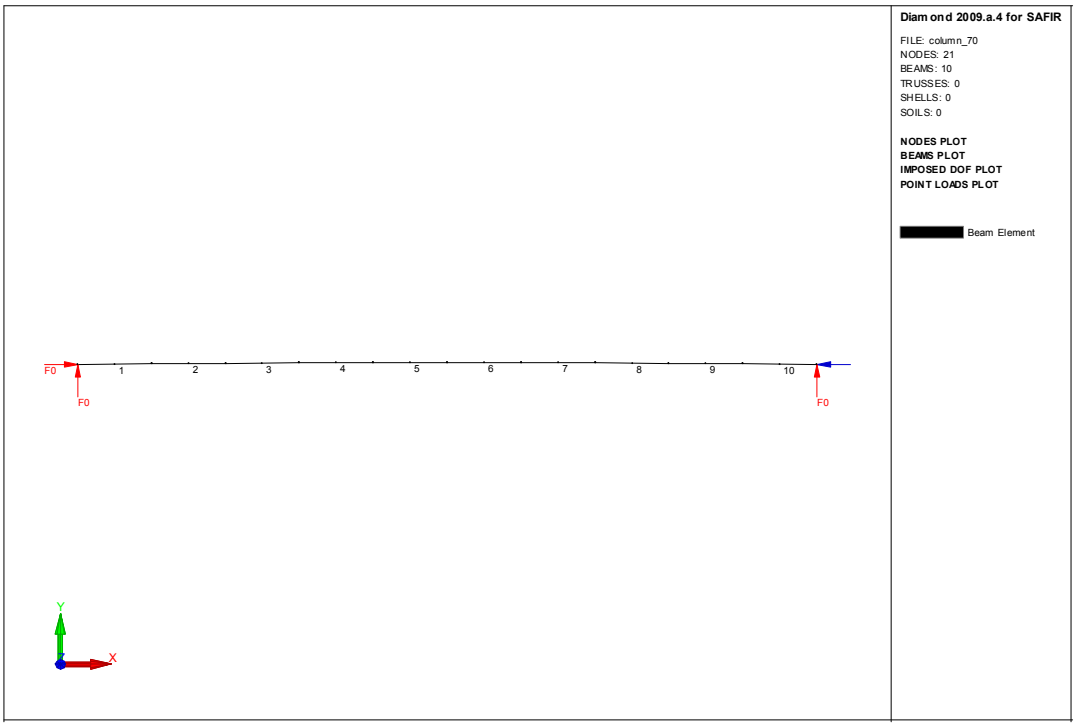

Figure 12. Columns C1, C2, C3 and C4 – longitudinal discretization (beam element)

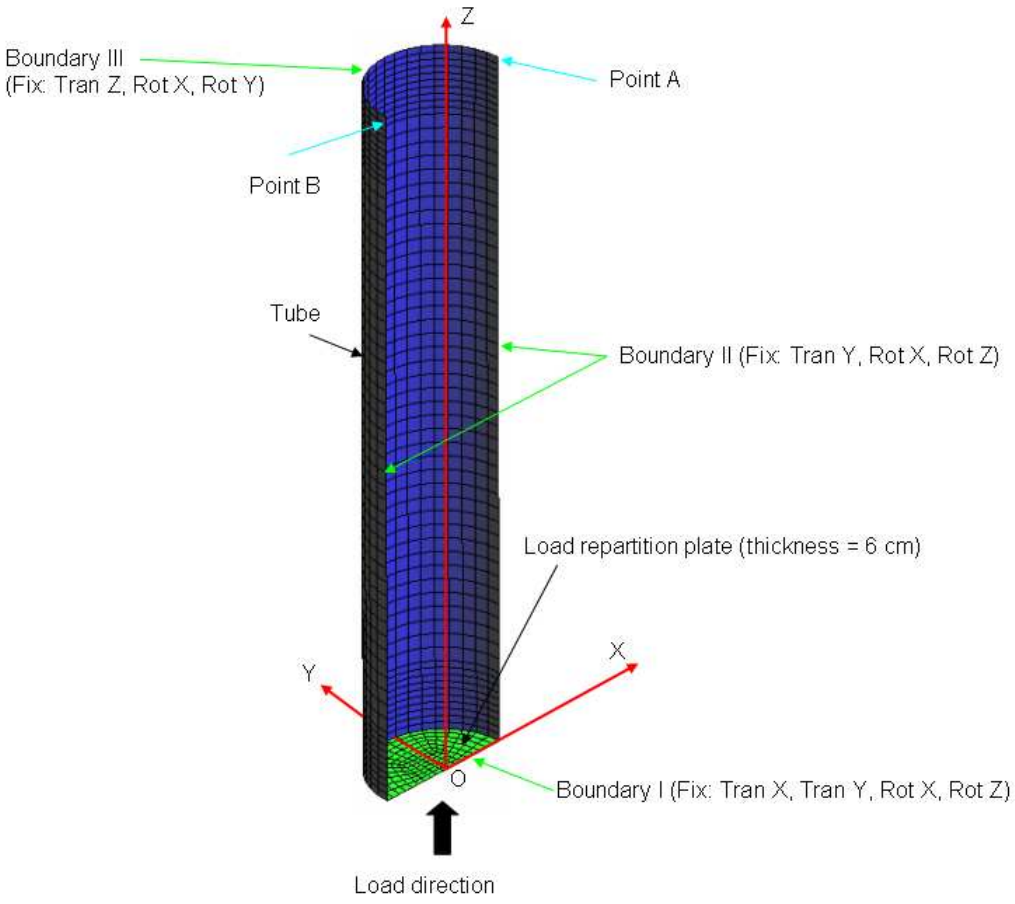

Figure 13. Columns C1, C2 and 3 – shell element discritization

Results and discussions

The fire resistances given by the numerical analysis are compared with the experimental one, the results are reported in Table 7. As an example, Figure 14 presents the deformation of the column C1 at the ultimate state, the global bucking is shown. It is observed that the numerical results are agreement with the experimental ones, in the both fire resistance and failure mode aspects.

Table 7. Comparison of the numerical results with the test results

Specimen	Fire resistances given by SAFIR (in minute)						Test results (in minute)
	Loading (a)		Loading (b)		Loading (c)		
	Shell	Beam	Shell	Beam	Shell	Beam	
C1	23	30	22,6	30	23,5	29	22
C2	21	22,5	21	22,5	21	21	20
C3	22	22	22	22	23	21,5	21
C4	-	104	-	104	-	84	108
The loading cases (a), (b) and (c) are described on Figure 8.							

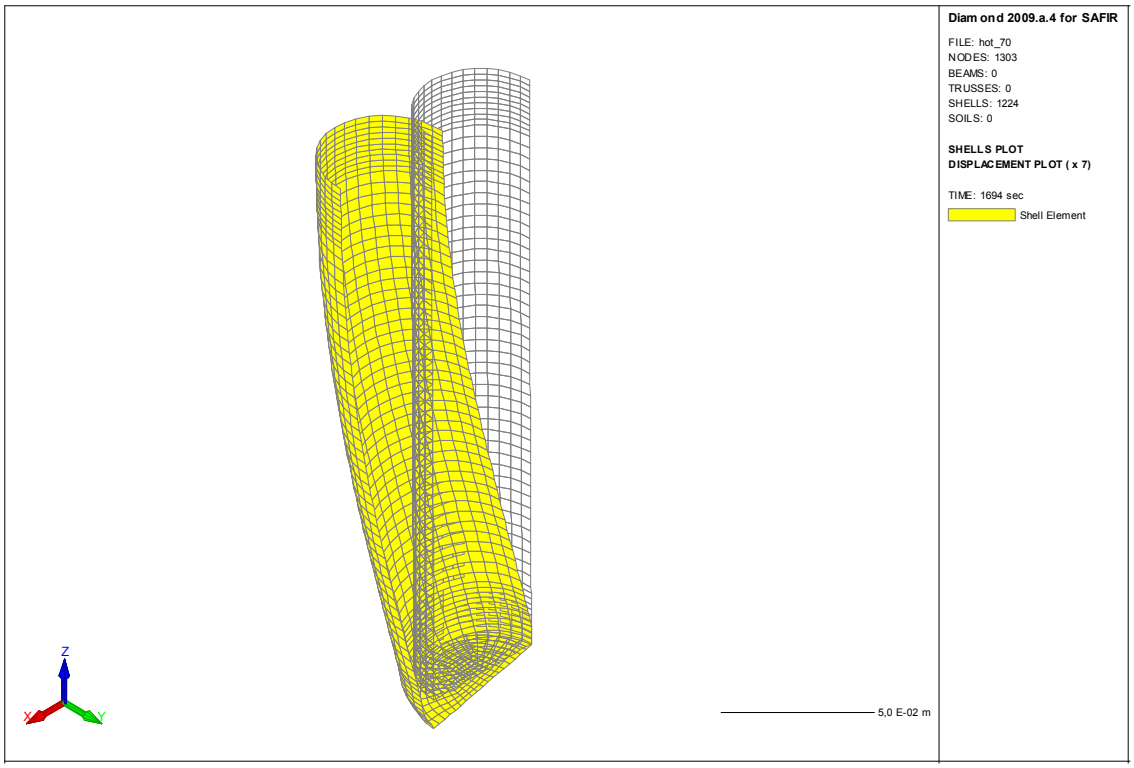

Figure 14. Column C1 (loading a, shell element) - deformation at the limit state (x7)

D.5.2.3. Simulation data of column-base and beam-to-column joints at normal temperature

D.5.2.2.1. *Hysteretic behaviour of both beam-to-column and column-base joints*

In order to investigate the response of the 5-storey prototype structure under seismic loading, it is fundamental the modelling of the hysteretic behaviour of both beam-to-column and column-base joints. The main steps were the following: i) analysis of test results to evaluate the location of plastic hinges; ii) choice of the model to take into account the behaviour, spread or concentrated plasticity; in those analyses concentrated plasticity was considered iii) choice of hysteretic models in order to simulate their actual behaviour iv) calibration of models parameters comparing numerical and experimental results. Both force-displacement of the actuator and moment rotation of plastic hinge were taken account. To calibrate the aforementioned models the whole structures tested were modelled, as shown in Figure 17, in Figure 22 and Figure 25.

Both beam-to-column and column-base joints were modeled using Bouc-Wen and pinching hysteretic models provided by Opensees, as shown in Figure 15 and Figure 16 rispectively. The two models were considered to operate in parallel, with exception of the innovative column-base joints where it was possible to model the hysteretic behaviour considering only one Bouc-Wen model. In the beam-to column joint and in the standard column-base seismic joint, the Bouc-Wen model provides the main part of actual behaviour, while the pinching model simulates slip due to damaged concrete and consequent hardening.

The calibration of the parameters took into account a unique model for the plastic hinge, in order to simulate tests subject to cyclic and random displacement protocols, respectively.

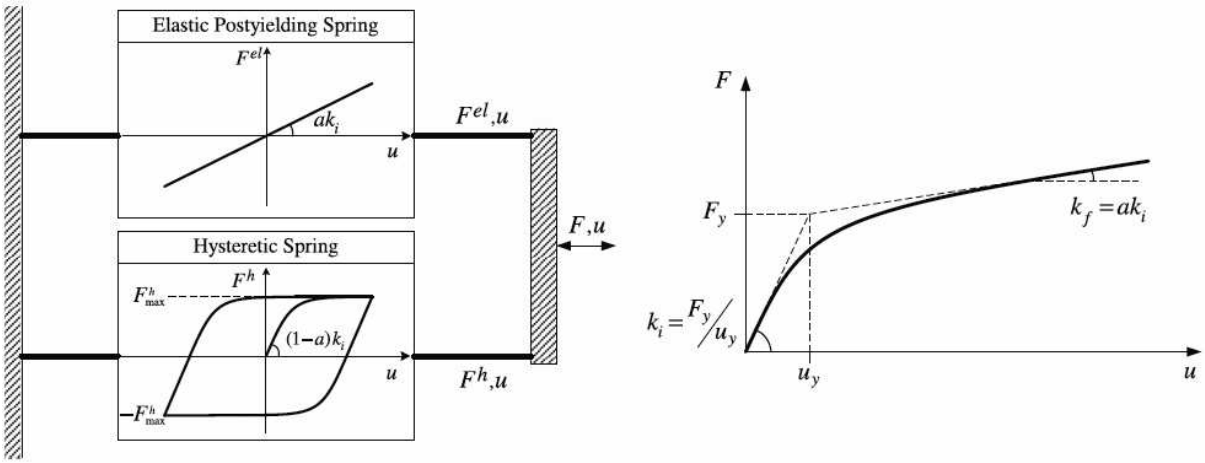

Figure 15. Bouc-Wen hysteretic model

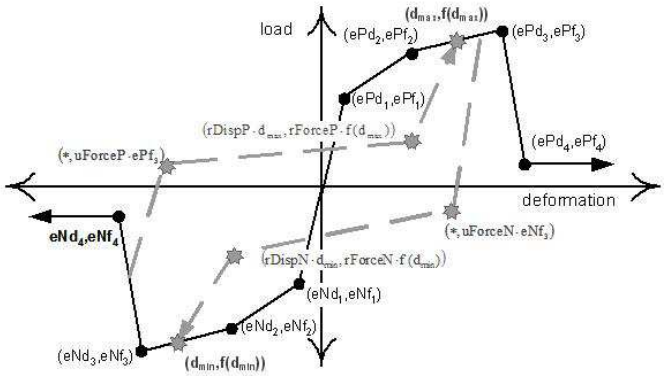

Figure 16. Pinching hysteretic model

Beam-to-column joints

Experimental results summarized in the WP3 exhibited the activation of plastic hinges in weak section between the beam ends and the plates welded to the column,

Figure 17 shows the model used in numerical analysis by Opensees, to calibrate the parameters of hysteretic behaviour. The numerical model was obtained by the idealization of actual tested structure.

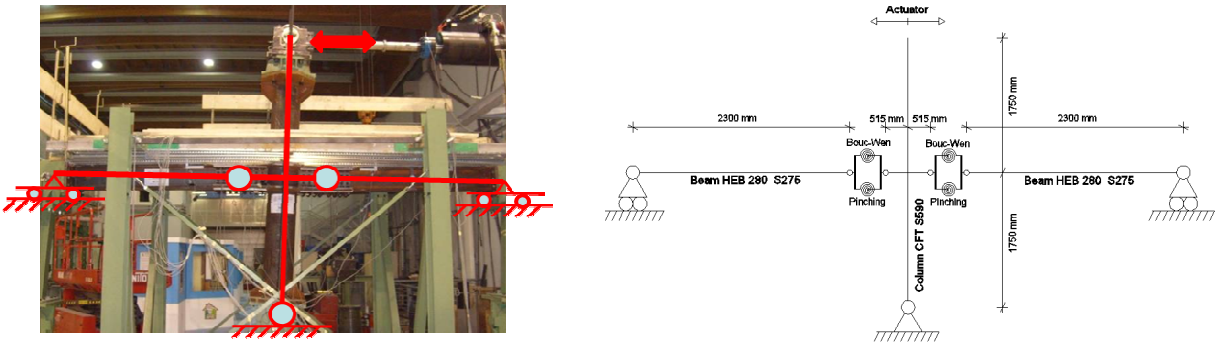

Figure 17. Model of tested beam-to-column joints

Figure 18 depicts the contribution of the two models used in order to simulate the hysteretic behaviour of beam-to-column joints; while Table 8 ÷ Table 10 summarizes values of model parameters.

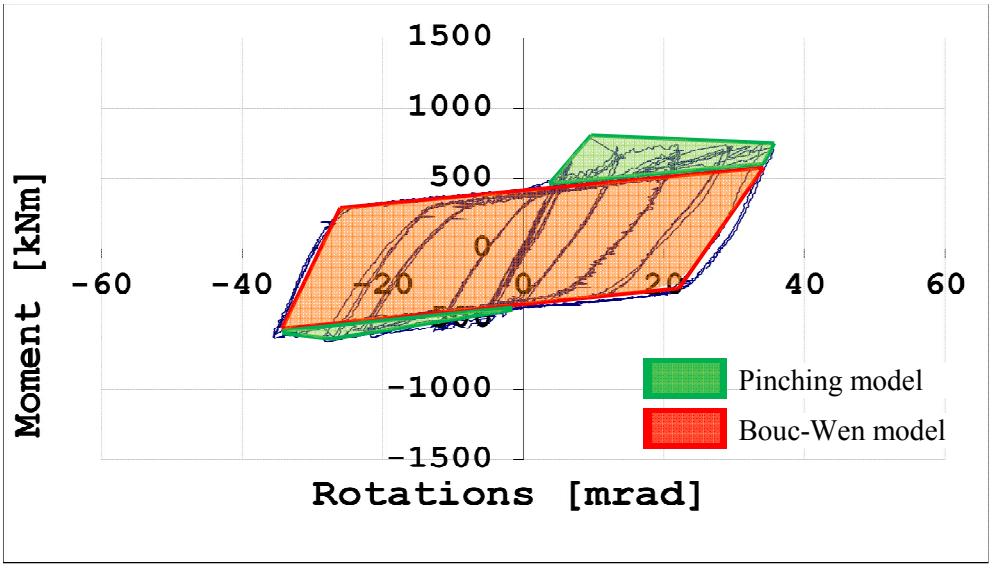

Figure 18. Hysteretic models of beam-to-column joints

Table 8. Bouc-Wen parameters of beam-to-column joints

α	k_0	n	γ	β	A_0	δA	δν	δη
0.065	0.88 E+11	1.76	6927	6927	1.00	0.00	0.00	0.00

Table 9. Pinching parameters of enveloping and target points of beam-to-column joint

ePf1	ePd1	ePf2	ePd2	ePf3	ePd3	ePf4	ePd4
375E+06	7E-03	333E+06	12E-03	295E+06	32E-03	180E+06	42E-03

eNf1	eNd1	eNf2	eNd2	eNf3	eNd3	eNf4	eNd4
-150E+06	-15E-03	-190E+06	-20E-03	-180E+06	-30E-03	-130E+06	-40E-03

rDispP	rForceP	uForceP	rDispN	rForceN	uForceN
0.50	0.25	0.25	0.50	0.25	0.25

Table 10. Pinching parameters of damage index of beam-to-column joint

gK1	gK2	gK3	gK4	gKLimit
0.25	0.35	0.40	0.20	0.50

gD1	gD2	gD3	gD4	gDLimit
0.50	0.50	2.00	2.00	0.50

gF1	gF2	gF3	gF4	gFLimit
0.70	0.00	0.60	0.70	0.90

gE	dmgType
10	energy

The comparison between experimental and numerical relevant to moment-rotation relationships of plastic hinges are shown herein.

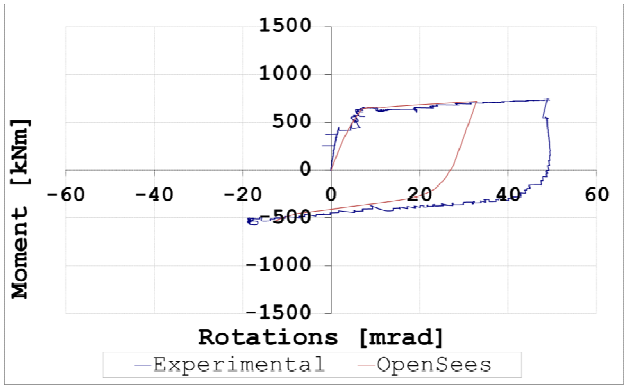

Figure 19. Moment-rotation relationship of beam-to-column joints subjected to monotonic testing

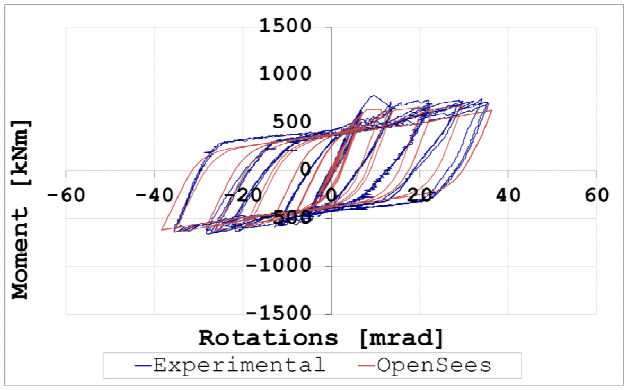

Figure 20. Moment-rotation relationship of beam-to-column joints subjected to cyclic testing

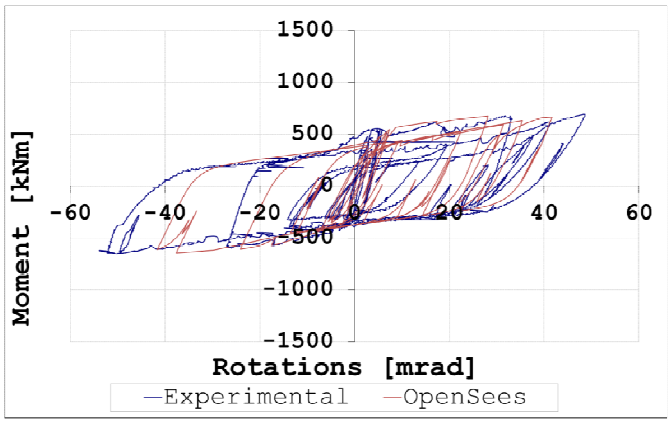

Figure 21. Moment-rotation relationship of beam-to-column joint subjected to random testing

Table 11 collects experimental and numerical energies dissipated by plastic hinges.

Table 11. Hysteretic energy value dissipate by beam-to-column joint

Test	Experimental [kJ]	Numerical [kJ]	Error [%]
Monotonic	19.062	19.961	4.71
ECCS	352.743	310.234	12.05
Random	154.415	144.289	6.56

Standard column-base joint designed for seismic loading

This joint was modelled by the presence of plastic hinge at the base of the column in correspondence of the grout between plinth of foundation and base plate, as shown in Figure 22.

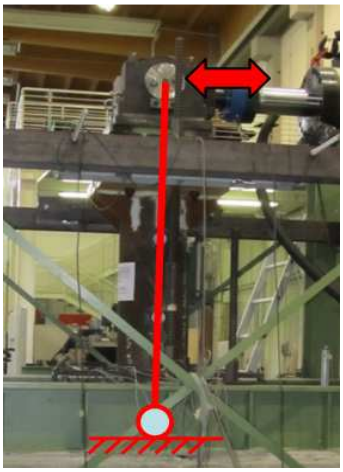

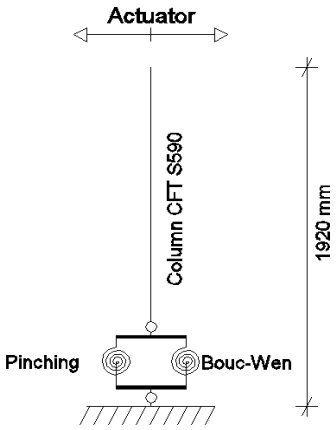

Figure 22. Model of standard column-base joint designed for seismic loading

Figure 23 depicts the contribution of the two models used in order to obtain the hysteretic behaviour of standard solution of column-base joints; while Table 12 ÷ Table 14 summarize values of parameters of models

Figure 23. Hysteretic models of standard column-base joint designed for seismic loading

Table 12. Bouc-Wen parameters of standard column-base joint designed for seismic loading

α	k_0	n	γ	β	A_0	δA	δν	δη
0.05	1.6E+11	2.00	117065.5	117065.5	1.00	0.9E-09	0.6E-09	13E-09

Table 13. Pinching parameters of envelope and target points of standard column-base joint designed for seismic loading

ePf1	ePd1	ePf2	ePd2	ePf3	ePd3	ePf4	ePd4
400E+06	3E-03	850E+06	10E-03	900E+06	50E-03	500E+06	8E-03

eNf1	eNd1	eNf2	eNd2	eNf3	eNd3	eNf4	eNd4
-400E+06	-3E-03	-850E+06	-9E-03	-900E+06	-50E-03	-400E+06	-8E-03

rDispP	rForceP	uForceP	rDispN	rForceN	uForceN
0.45	0.30	-0.375	0.4531	0.30	-0.3929

Table 14. Pinching parameters of damage index – standard column-base joint designed for seismic loading

gK1	gK2	gK3	gK4	gKLimit
0.25	1.00	1.00	1.00	0.80

gD1	gD2	gD3	gD4	gDLimit
0.80	0.80	0.80	0.80	1.00

gF1	gF2	gF3	gF4	gFLimit
1.00	1.00	1.00	1.00	0.25

gE	dmgType
10	Energy

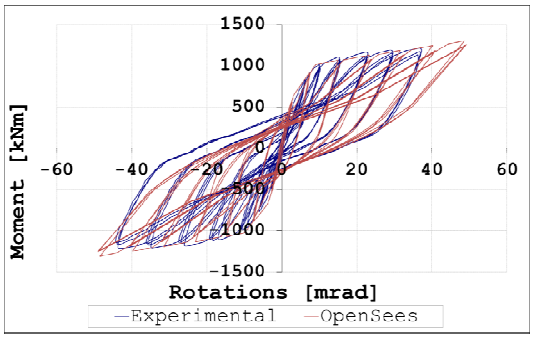

a)
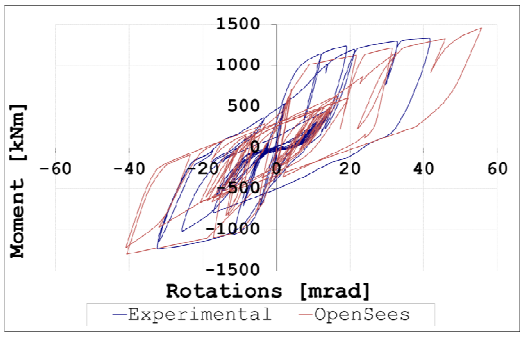

b)

Figure 24 Moment-rotation relationship for standard column-base joint: a) cyclic test; b) random test

Table 15 gathers both the experimental and numerical energy dissipated by plastic hinges

Table 15. Hysteretic energy value dissipate by Standard seismic column-base joint

Test	Experimental [kJ]	Numerical [kJ]	Error [%]
ECCS	352.011	413.118	14.79
Random	110.126	148.160	25.67

Innovative column-base joint designed for seismic loading

The joints were characterized by the presence of a plastic hinge at the base of the column in correspondence of the grout between plinth of foundation and base plate, as shown in Figure 22.

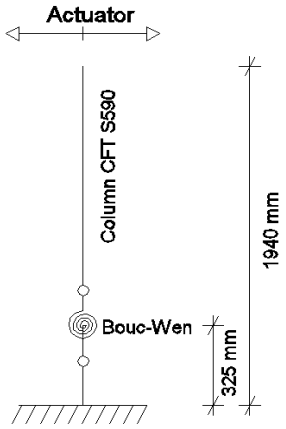

Figure 25. Model of standard column-base joint designed for seismic loading

Figure 26 depicts the contribution of the two models used in order to obtain the hysteretic behaviour of beam-to-column joint; while Table 16 summarizes the values of model parameters

Figure 26. Hysteretic models of innovative column-base joint designed for seismic loading

Table 16. Bouc-Wen parameters of standard column-base joint designed for seismic loading

α	k_0	n	γ	β	A_0	δA	δν	δη
0.28739	0.40E+11	3.30	97514.2	97514.2	1.00	4E-10	0.1E-11	2.5E-11

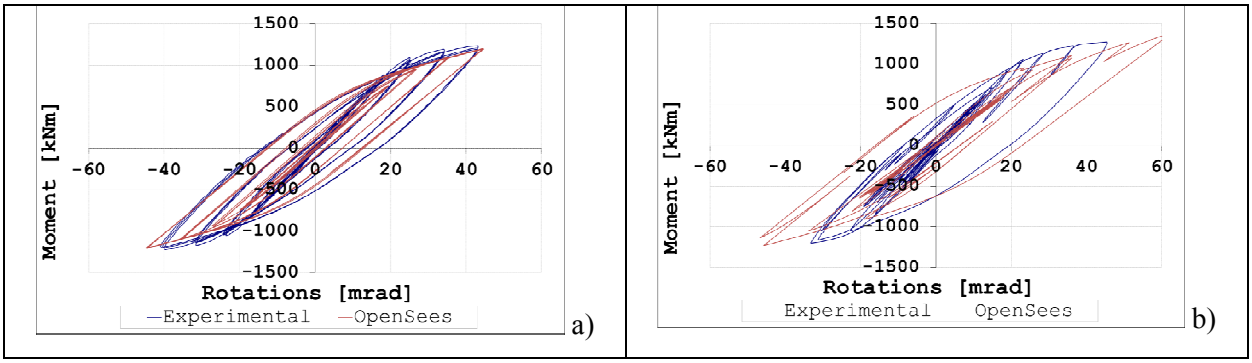

Figure 27 Moment-rotation relationship for innovative column-base joint: a) cyclic testing; b) random testing

Table 17 compares the experimental and numerical energy dissipated by the plastic hinge.

Table 17. Hysteretic energy value dissipate by Innovative seismic column-base joint

Test	Experimental [kJ]	Numerical [kJ]	Error [%]
ECCS	275.885	245.205	12.51
Random	83.292	112.058	25.67

D.5.2.2.1. Mechanical behaviour of a plinth relevant to an innovative seismic joint

Formulae proposed in EN 1992-1-1 (2005) [8] for pocket foundations consider rectangular columns embedded in the plinth, as showed in Figure 28. The innovative solution realised by a circular column requires the investigation of Strut & Tie mechanisms that transfer forces between the column and the foundation. The analysis of the mechanical behaviour of the innovative column-base joint requires a 3D numerical model set by the ABAQUS program. The calibration of the 3D numerical model proposed required elevated computational costs due to : i) non-linearity of the problem consequent to damage of the concrete in tension; ii) presence of constrains among different parts of joints as column surface and concrete block or the base plate and the grout. Figure 29 shows the large number of rebars present in the FE model generated by ABAQUS software.

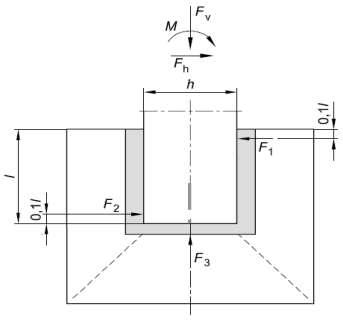

Figure 28. Plinth with a rectangular column

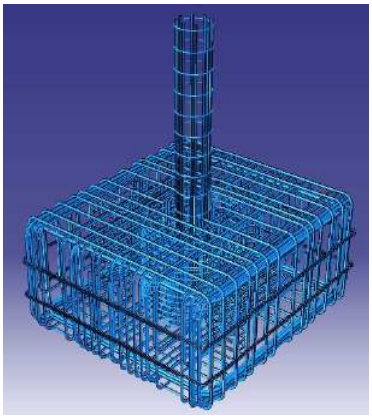

Figure 29. Re-bars in the FE model of a column-base joint

Analyses were conducted with FE program ABAQUS by means of a Standard Analysis. Column-base were subject to cyclic tests only; therefore, the envelope of force-displacement relationship was considered. The model was calibrate applying monotonic displacement and comparing: i) the horizontal force provided by FE model with the one recorded by the actuator in order to apply the same

displacement during tests, as shown in Figure 30; ii) the forces recorded during the test by strain gauges welded on the rebars located in the plinth.

Numerical results were satisfactory and in agreement with experimental data till the onset of yielding. After the yielding the numerical response showed higher stiffness w.r.t. actual response. It was very difficult to take account in the model the damage of the grout owing to cyclic loading, between the steel column and the foundation block.

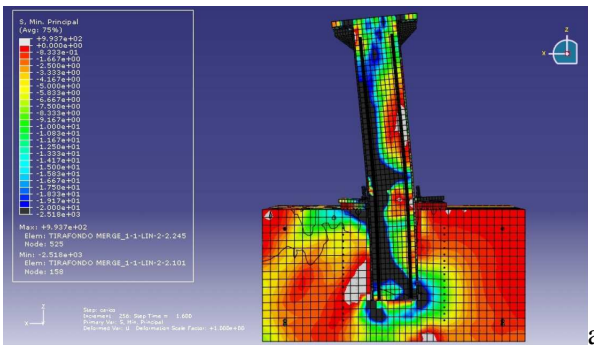

a)

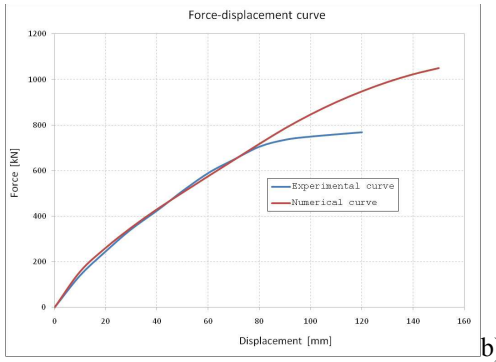

b)

Figure 30. Innovative column-base joint: a) distribution of stresses in the specimen; b) comparison between numerical and experimental data

The resulting mechanism was endowed with: i) two frontal struts along the diagonal of the plinth with a rectangular section of about 400 x 360 mm; ii) a rear strut parallel to the face of the plinth with a rectangular section of about 500 x 400 mm. Figure 31 shows the geometry of the struts in the plinth obtained by means of FE analysis.

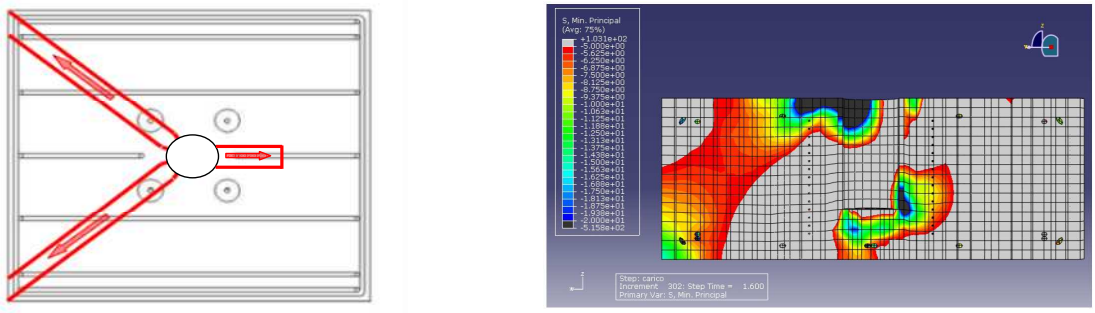

Figure 31. Strut & tie mechanism and distribution of compressive principal stresses for the plinth of the innovative column-base joint

D.5.2.4. Numerical analysis of connections in fire condition

This section presents the numerical analysis for the connections (beam-to-column joints and column bases) that were tested in WP4. The detail of the geometries and the materials of the specimens and also the test descriptions (location of thermocouples, location of displacement transducers, loading sequences, etc.) can be found in Deliverable D4. It concerns two static joints (J11 and J12), two seismic joints (J21 and J22), one static column base (CB1) and two seismic column bases (CB2, CB3).

Thermal analysis for static joints

In the fire condition, it can say that the critical zones of the static joints are the bolts, plates and the columns, not the rebar that are protected by the concrete. Moreover, there are not much influences of the slap to the temperature development in the steel parts (bolts, plates and column).By consequence, the use of 3D solid model for the whole of joints (Figure 32) may be not necessary, as it is expensive in the level of computation cost. In order to simulate the temperature in the “bolt” zone, the model as the show on Figure 33 can be adopted. The 2D model on Figure 34 may be used for the vertical plate and the column. Using the ISO FIRE in the model, the temperature development in the different zones given

by proposed models are compared with the test ones (Figure 35 to Figure 38). The agreements are shown and it point out that the used models (Figure 33 and Figure 34) can be applied to simulated temperature in the static joints under fire loading.

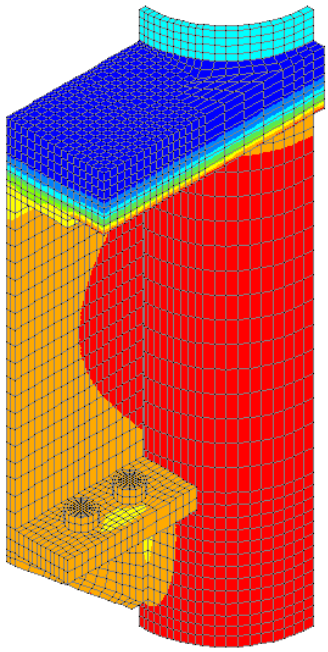

Figure 32. Static joint - 3D model in thermal analysis for the whole of static joints

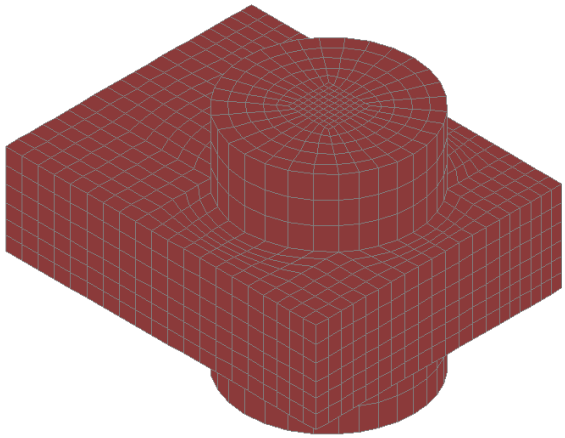

Figure 33. Static joint - 3D model for the “bolt” zone

Figure 34. 2D model with (“VOID” declaration) for the vertical plate and the tube

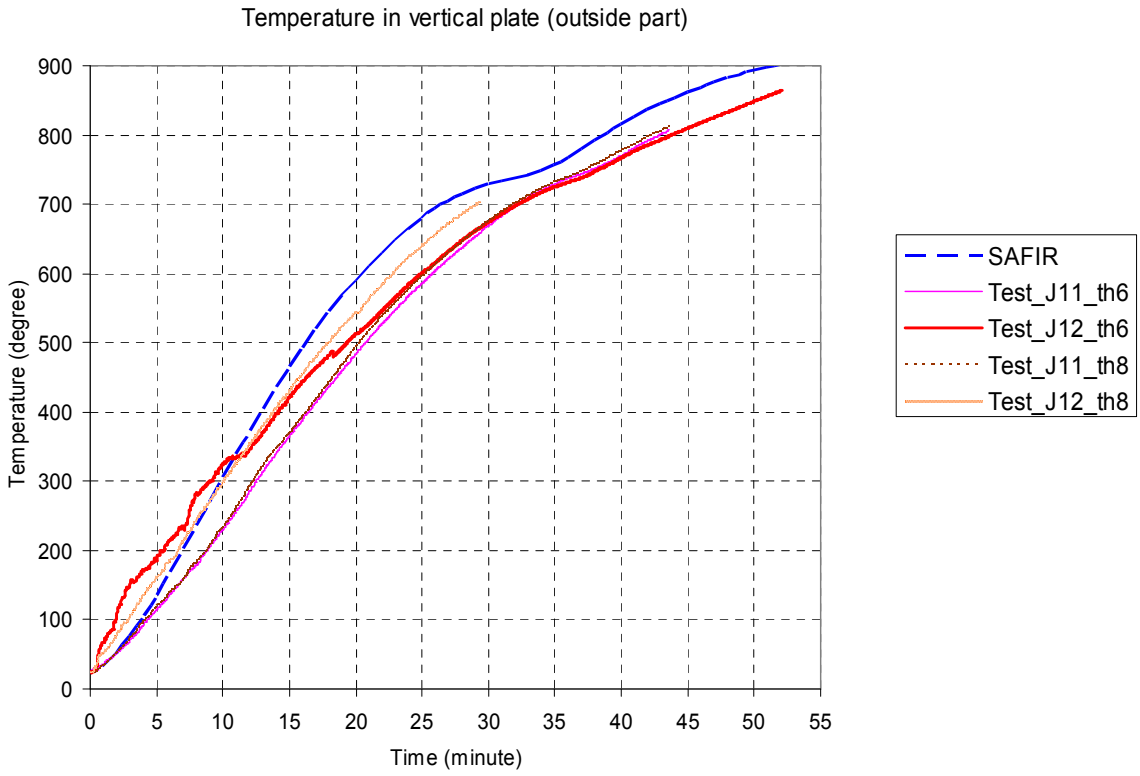

Figure 35. Static joint – comparison of temperature in the vertical plate (outside part)

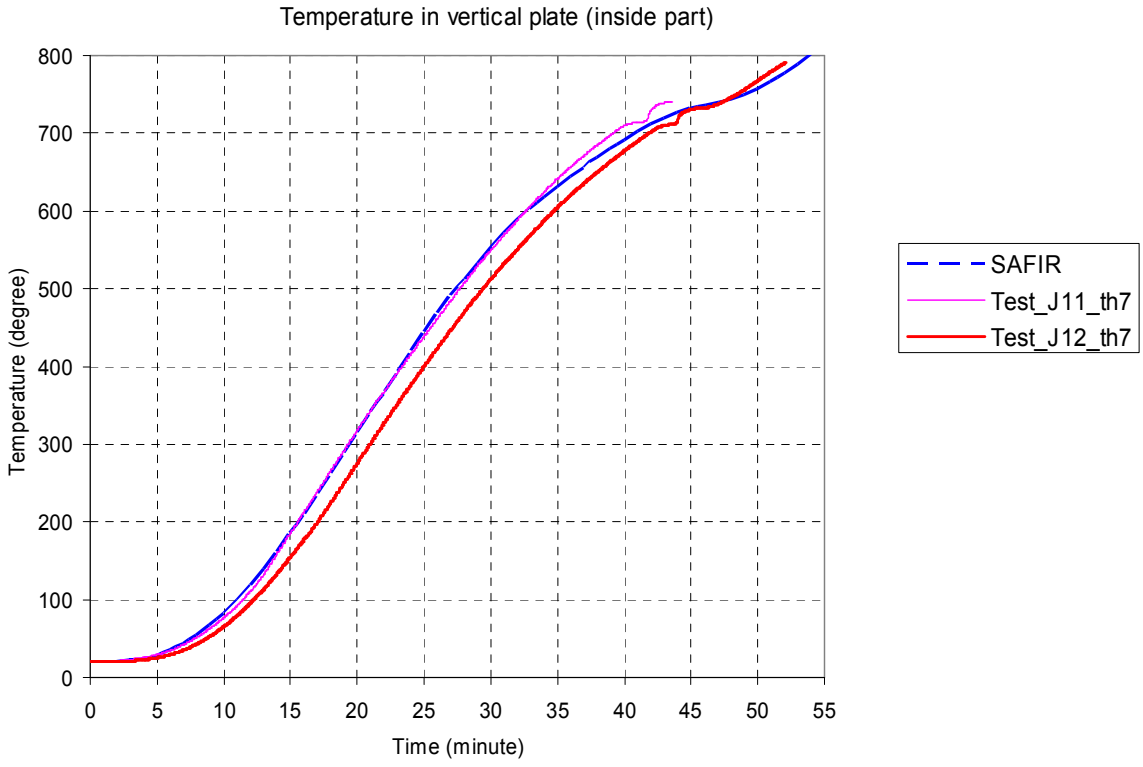

Figure 36. Static joint – comparison of temperature in the vertical plate (inside part)

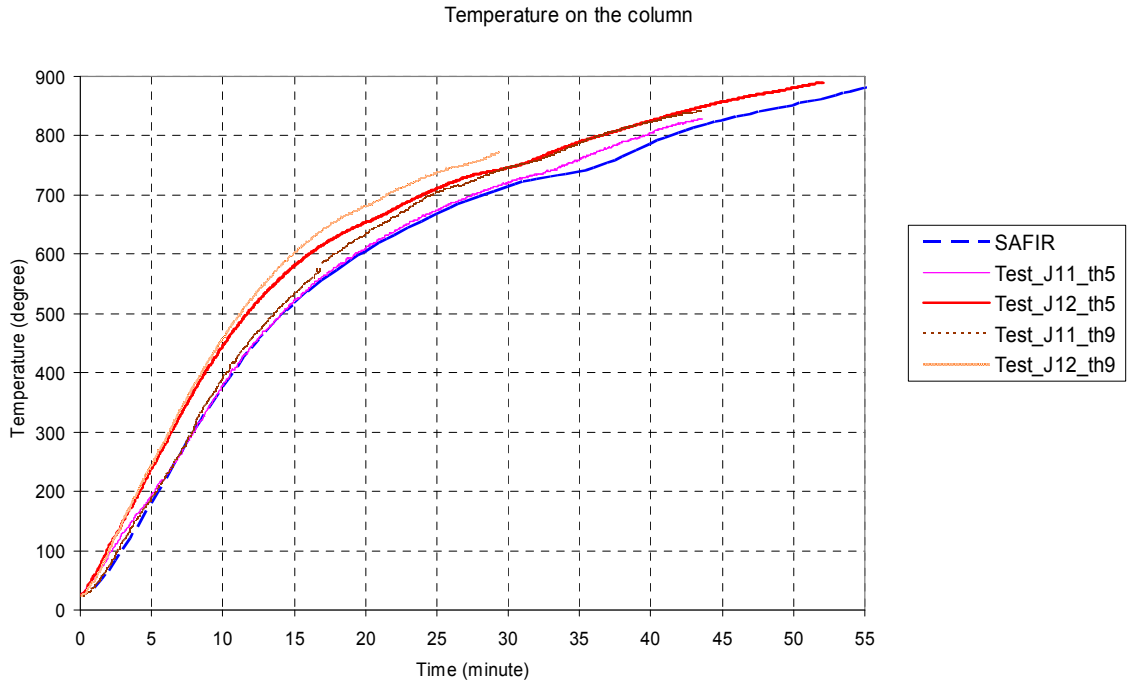

Figure 37. Static joint – comparison of temperature in the column

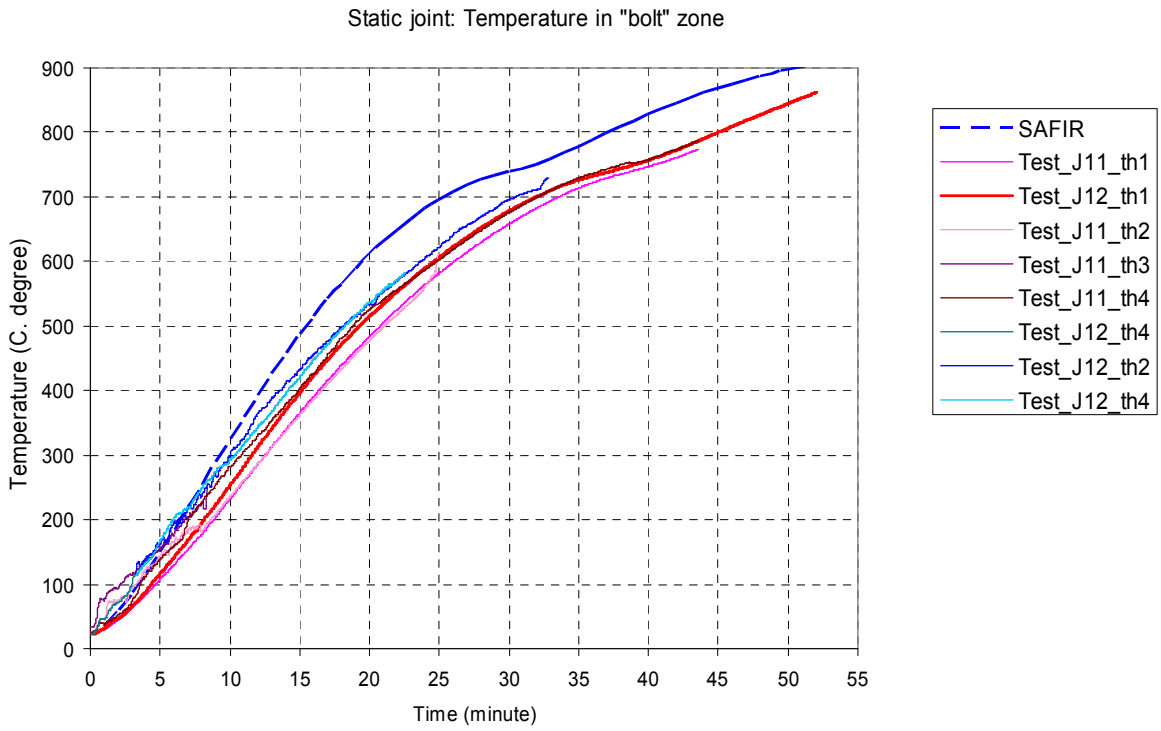

Figure 38. Static joint – comparison of temperature in the “bolt” zone

Thermal and mechanical analysis for seismic joints

Thermal analysis

A 3D solid model (Figure 39) is developed to simulate the temperature in the steel parts (beam, bolts and plates) of the seismic joints. On the other hand, 2D model is adopted to predict the temperature in

the rebars of the concrete slap (Figure 40). In the practices, the steel parts may be grouped into three zones (Figure 39), the differences of temperature within each zone can be neglected.

The numerical results are comparison with the experimental ones (Figure 41 to Figure 44). In general, the temperatures given by the numerical analysis are greater than the one of the tests, in particular with respect to the temperature in the rebar. The reason is maybe the influence of the composite column (absorb much of energy) that is not modelled in the model. However, the numerical analysis gives the conservative side.

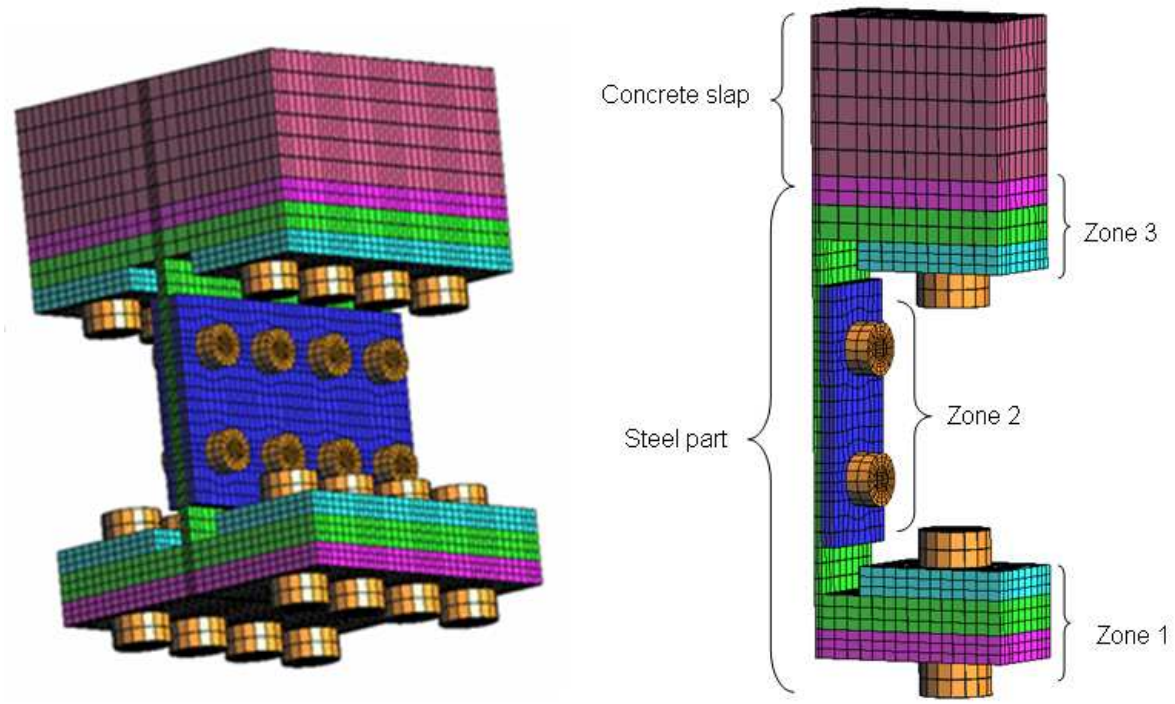

Figure 39. FE modelling of the seismic joints in the thermal analysis

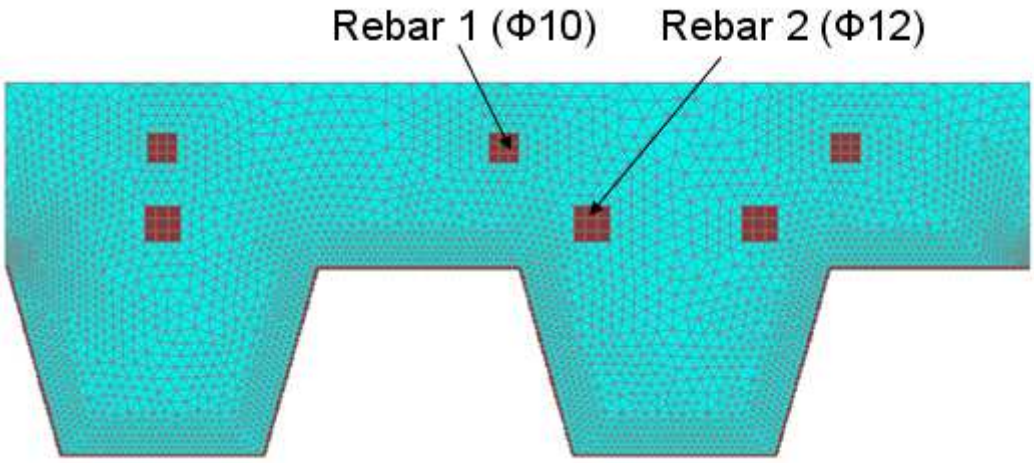

Figure 40. FE modelling for concrete slap of seismic joints

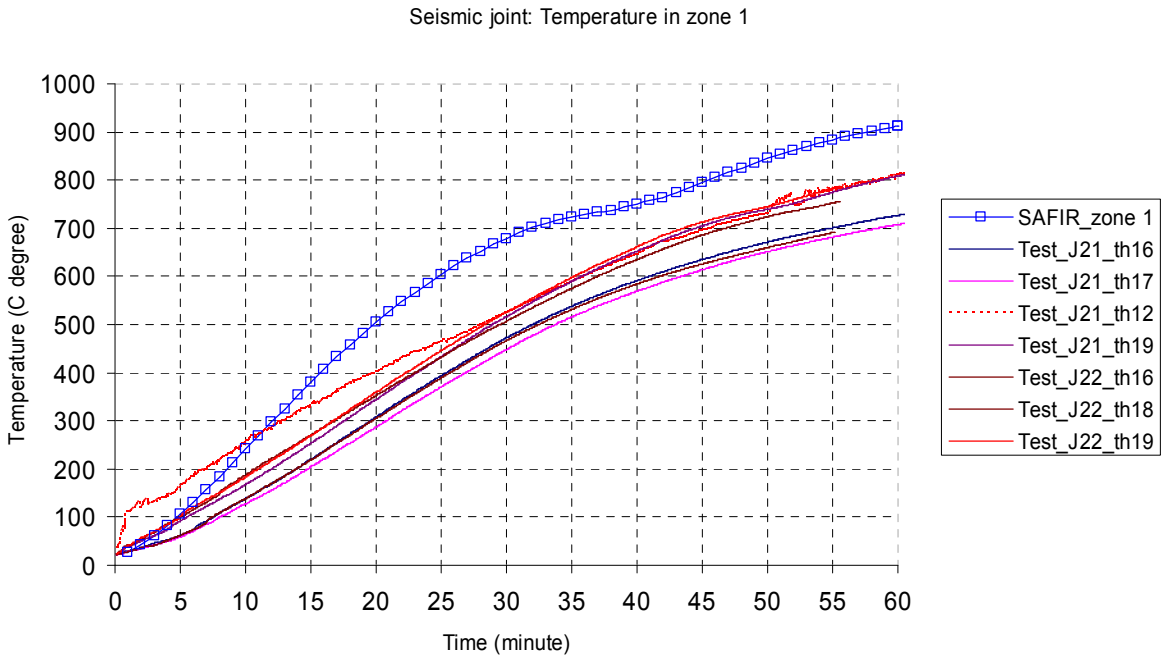

Figure 41. Seismic joint – comparison of temperature in zone 1

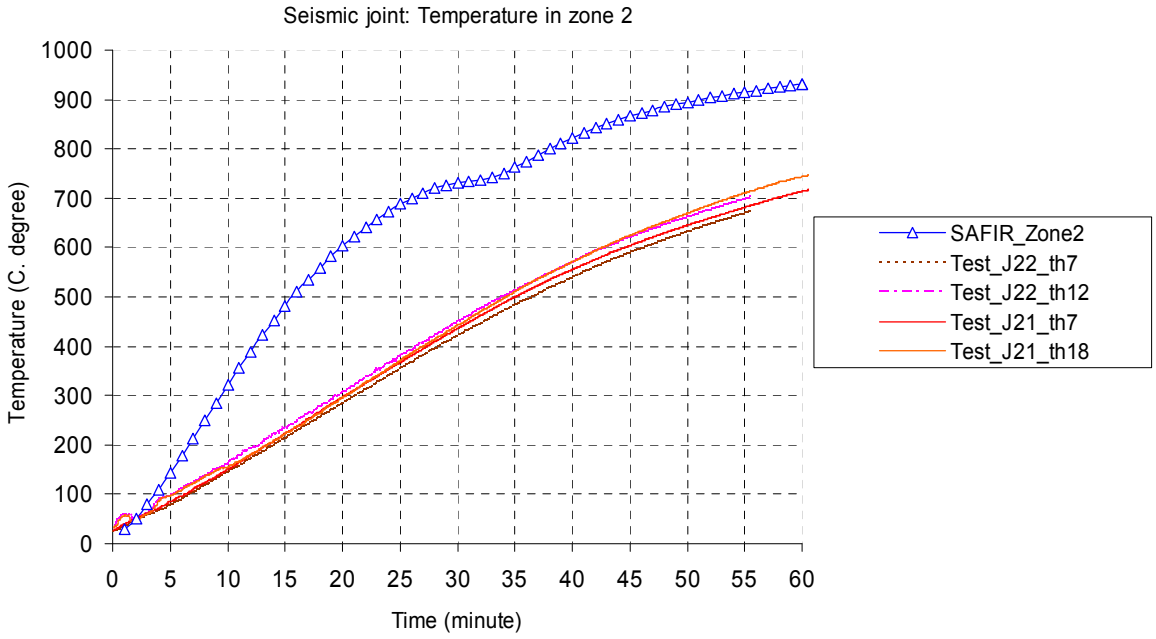

Figure 42. Seismic joint – comparison of temperature in zone 2

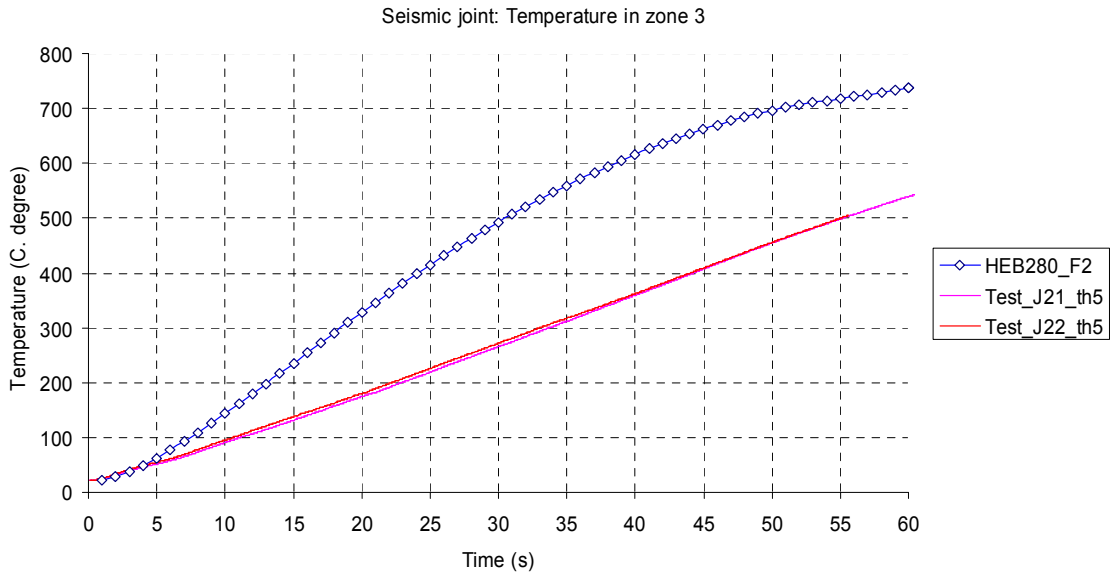

Figure 43. Seismic joint – comparison of temperature in zone 3

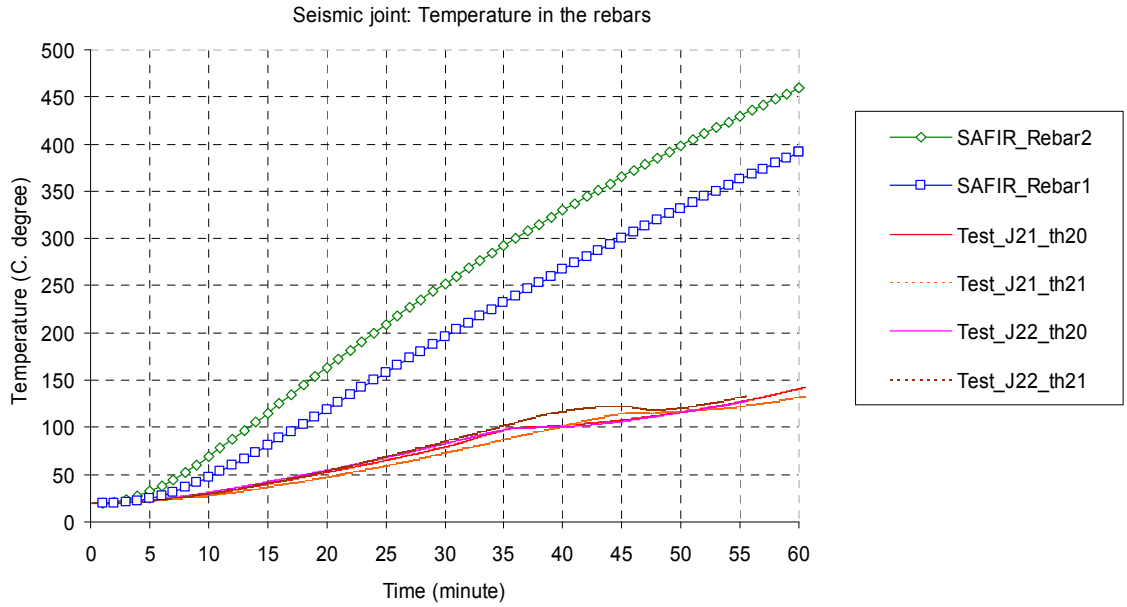

Figure 44. Seismic joint – comparison of temperature in rebars

Mechanical analysis

It is complicated to use 3D solid model for simulating the mechanical behaviour of the joints, so a model by using beam elements is proposed (Figure 45). In this model, the section of beams is varied according to the actual configuration of the joints, the shear deformation of the bolts are omitted. The temperature developments recorded by the thermocouples in the tests are used to impose the temperature in the corresponding zones of the sections.

The load point displacements given by SAFIR are presented on Figure 46 and Figure 47 which are compared with the experimental ones (Figure 48 and Figure 49). It can observe that the fire resistance is good in agreement between the calculation and the tests. However, the time-displacement curves are more ductility than the numerical ones.

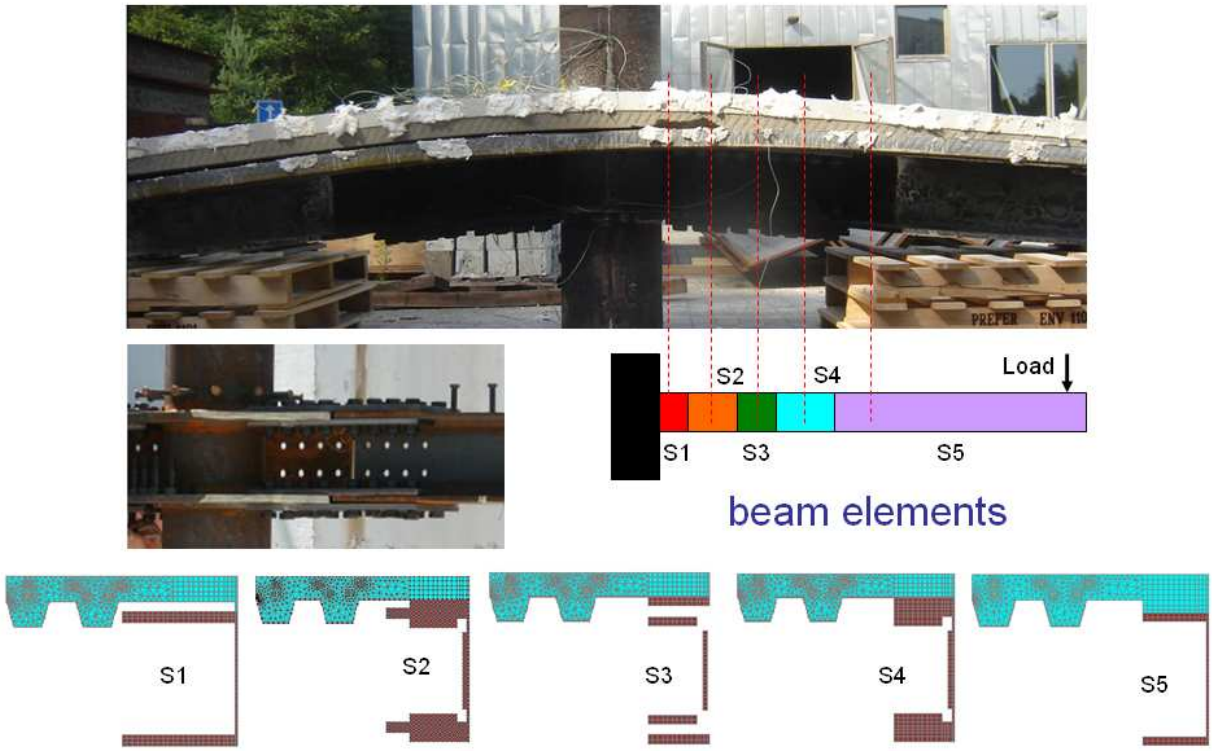

Figure 45 . Mechanical modelling of the seismic joints

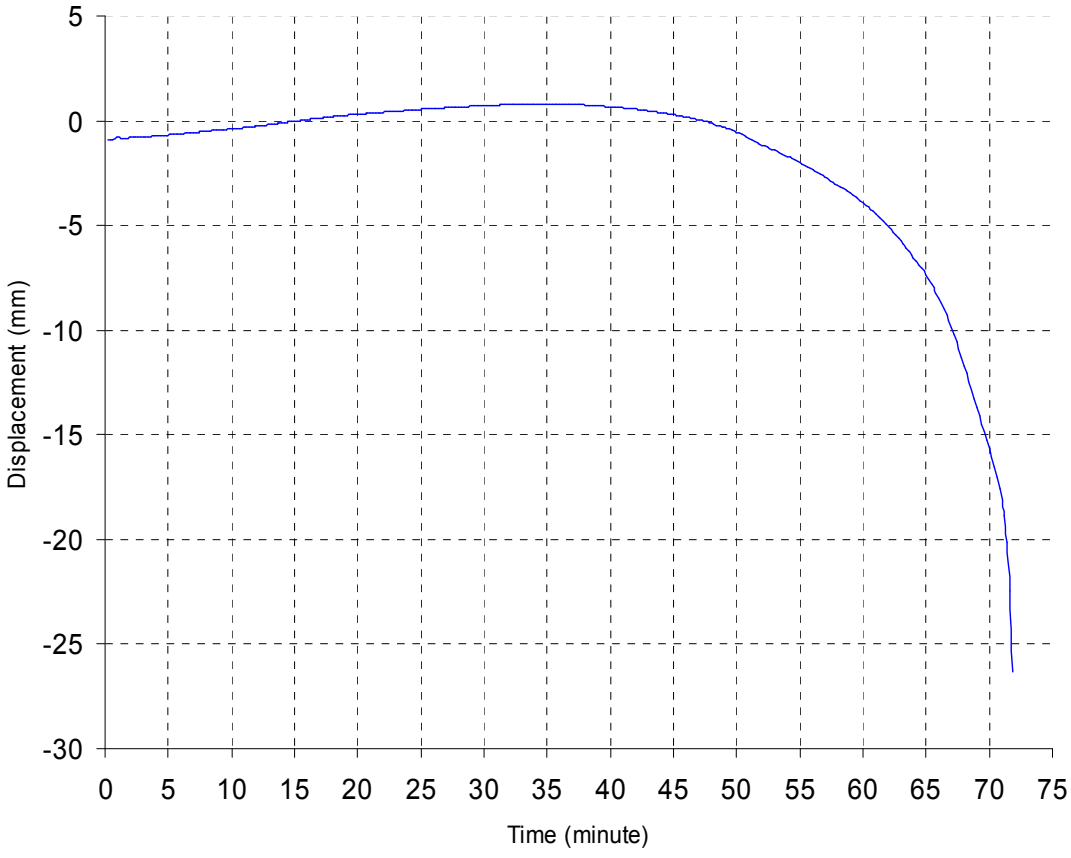

Figure 46. Seismic joint J21– point load displacement given by SAFIR

Figure 47. Seismic joint J22– point load displacement given by SAFIR

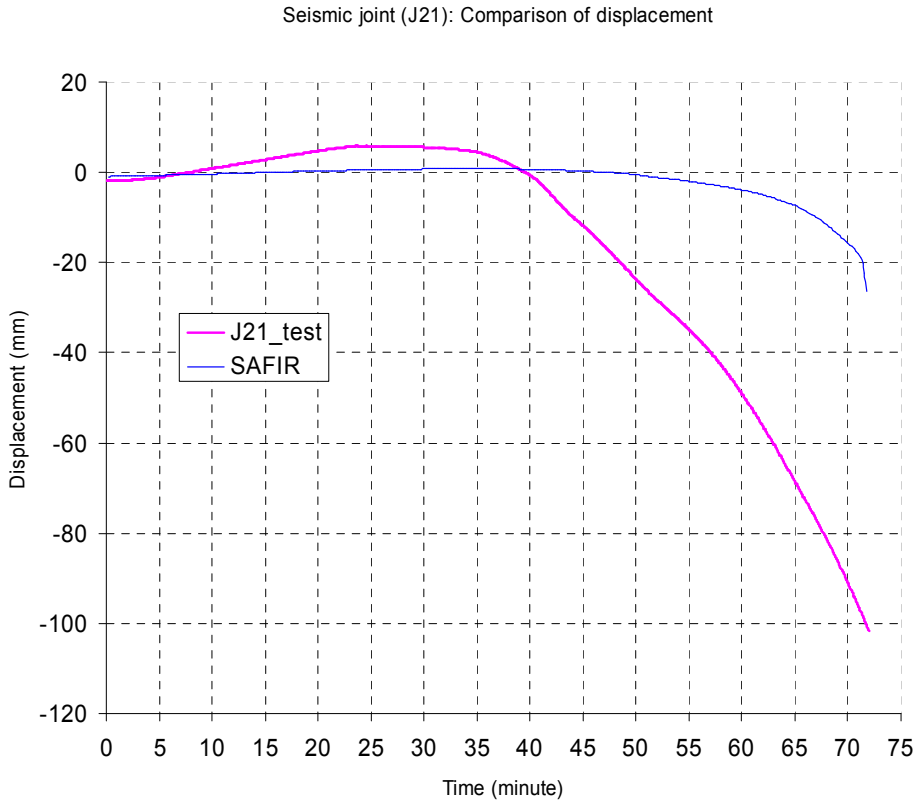

Figure 48. Seismic joint J21–comparison of displacement

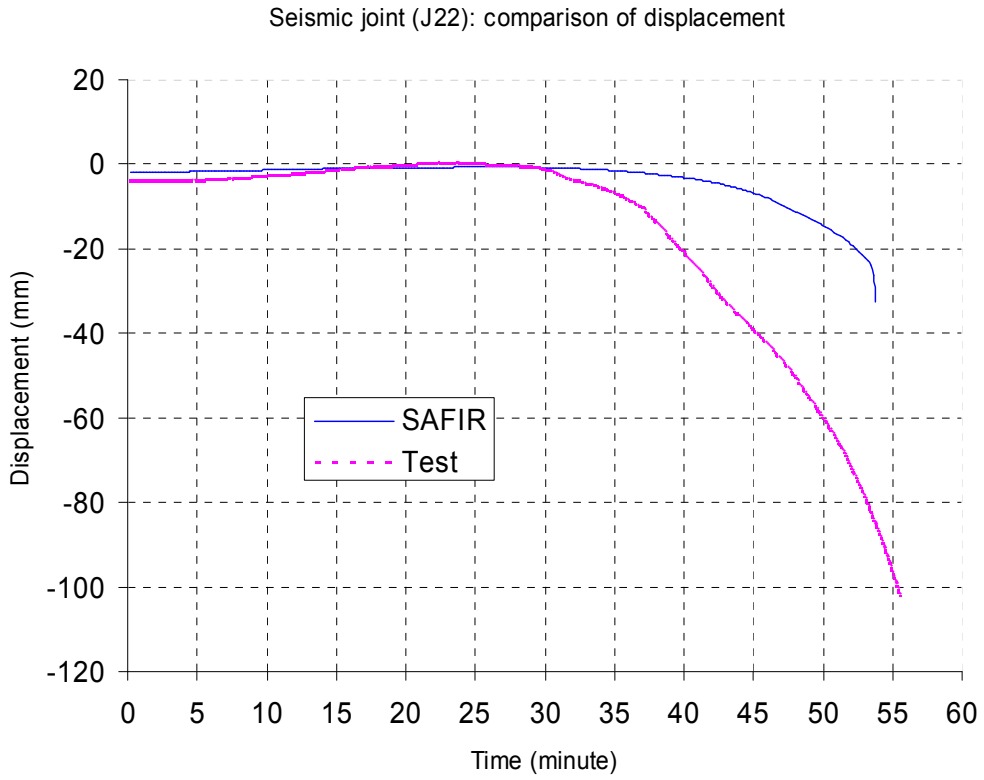

Figure 49. Seismic joint J22–comparison of displacement

Thermal and mechanical analysis for column bases

Thermal analysis

Figure 50 and Figure 51 are respectively shows the developed model for CB2 and CB3. For the moment, the temperatures in some zones given by the FE model are compared with the test results (Figure 52 and Figure 53), the agreement is shown.

Noting that the thermal analysis results for the end plate and the bolts of CB3 can be used for CB1 (static column base) while the temperature in the steel column of CB1 may be computed as in the isolated steel column in taking into account the influence of the foundation..

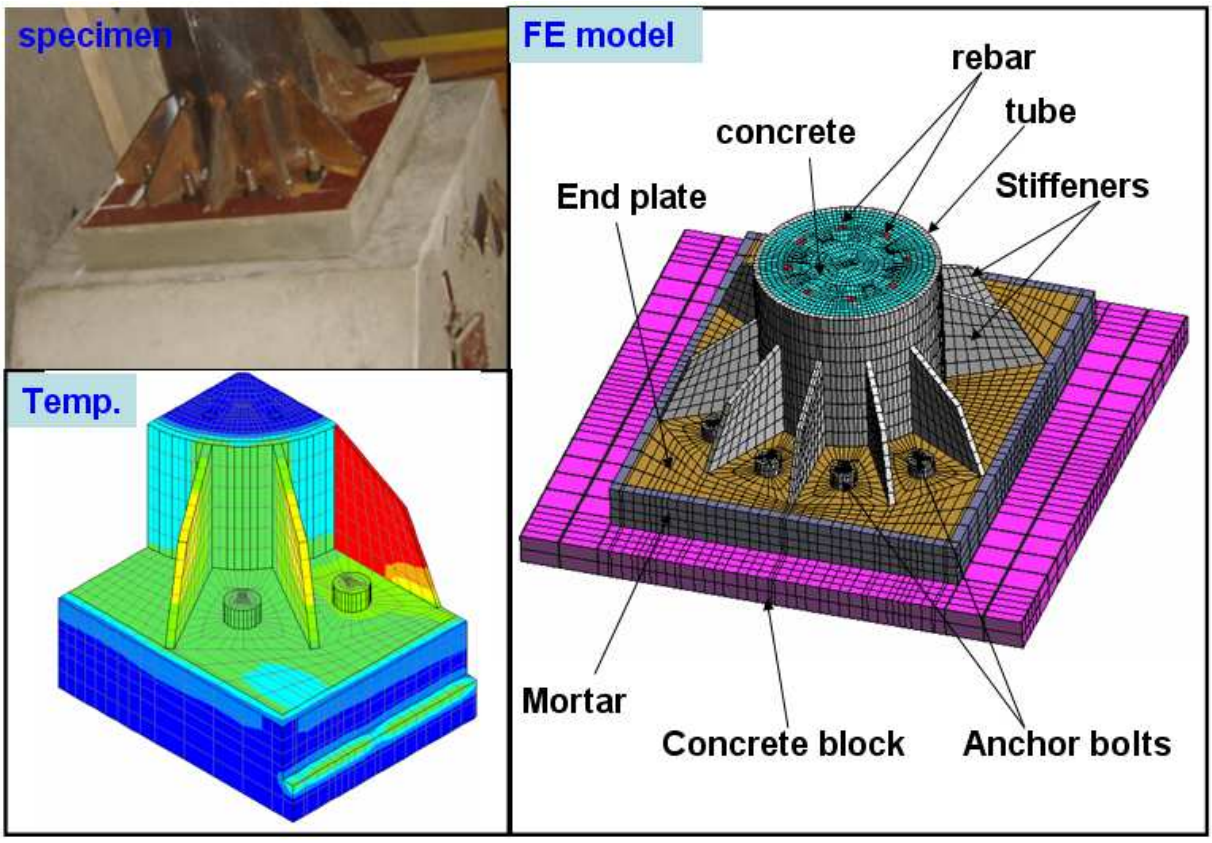

Figure 50. EF modelling in thermal analysis of column base CB2

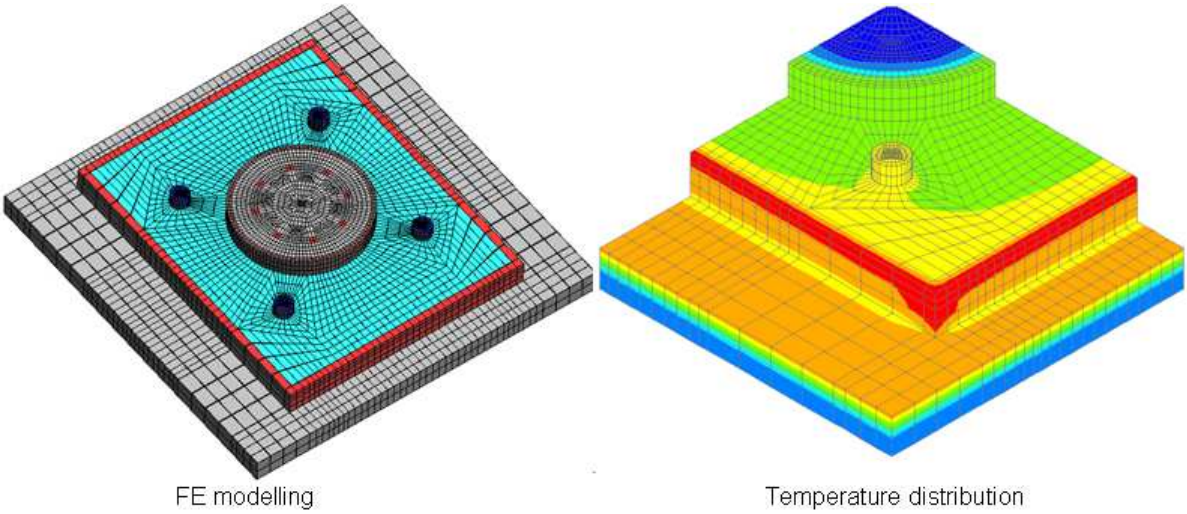

Figure 51. EF modelling in thermal analysis of column base CB3

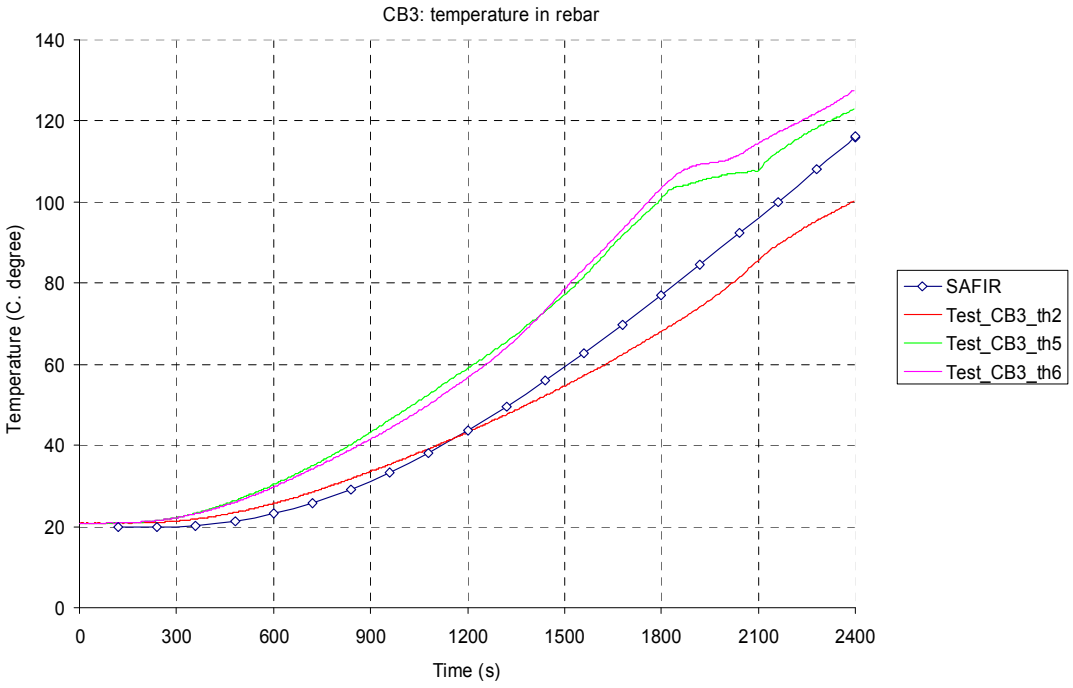

Figure 52. Seismic column base - comparison of temperature in rebar

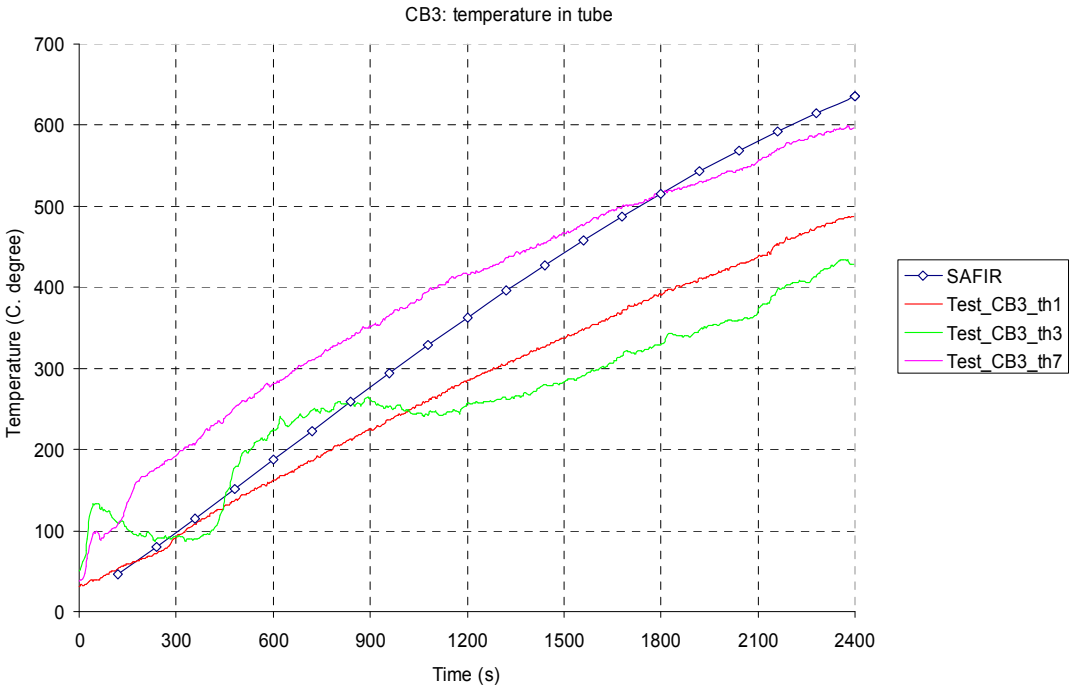

Figure 53. Seismic column base - comparison of temperature in steel tube

Mechanical analysis

In the fire condition, after about 30-40 minutes, it can say that the capacities of steel parts (stiffeners, end plate and bolts) strongly decrease, while the composite column can resist in more of time. Therefore, the behaviour of the column bases is quite similar to the behaviour of the composite column clamped in the foundation (Figure 54). This observation is in agreement with the experimental tests:

CB2 and CB3 are very different in the level of steel parts (end plate thickness, number of bolts and present of stiffeners), but the behaviour in fire are similar (Figure 55 and Figure 56). Noting that CB2 and CB3 were tested under the same condition (as ISO fire, test set-up and load value). From the remark, the model using beam element (end plate, bolts and stiffeners are neglected, only composite column is considered) is proposed to simulate the tests on CB2 and CB3 specimens (Figure 57). In this model, the temperature in the tube and the rebar are imposed by the temperature recorded by the thermocouples. The time-displacement curves given by the SAFIR is reported on Figure 58 (SAFIR_V is the vertical displacement of point C while SAFIR_H is the horizontal displacement of the point E, see Figure 57). The fire resistances of the column bases are well predicted by the present model while the time-displacement curves of the tests are more ductility than the numerical one (Figure 59).

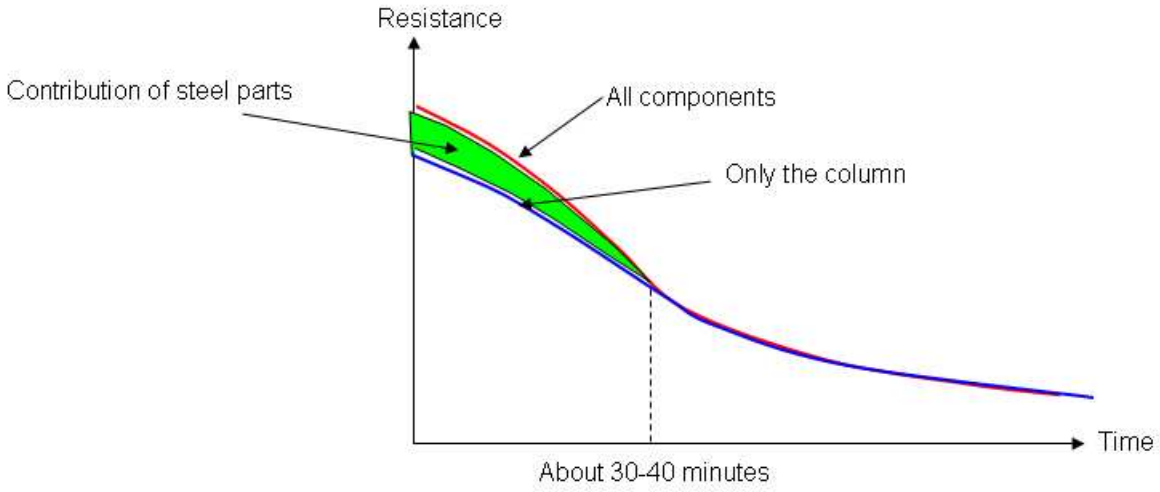

Figure 54. On the resistance in fire of column base with composite column

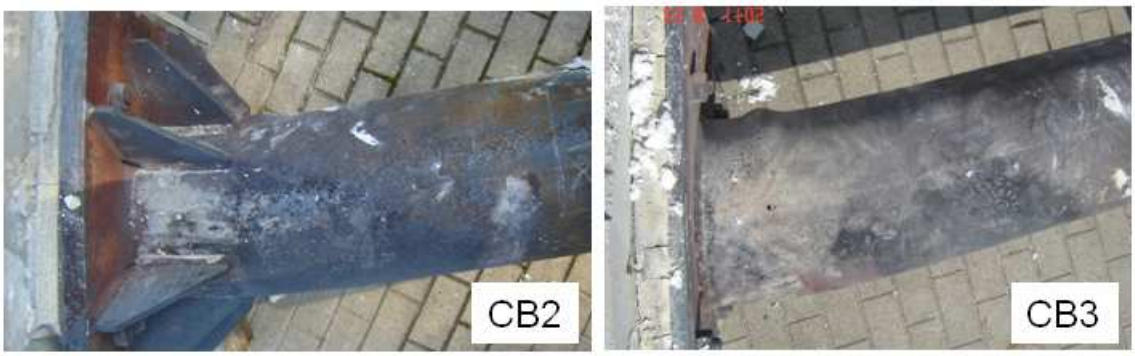

Figure 55. The similar (global level) of the failure modes of CB2 and CB3

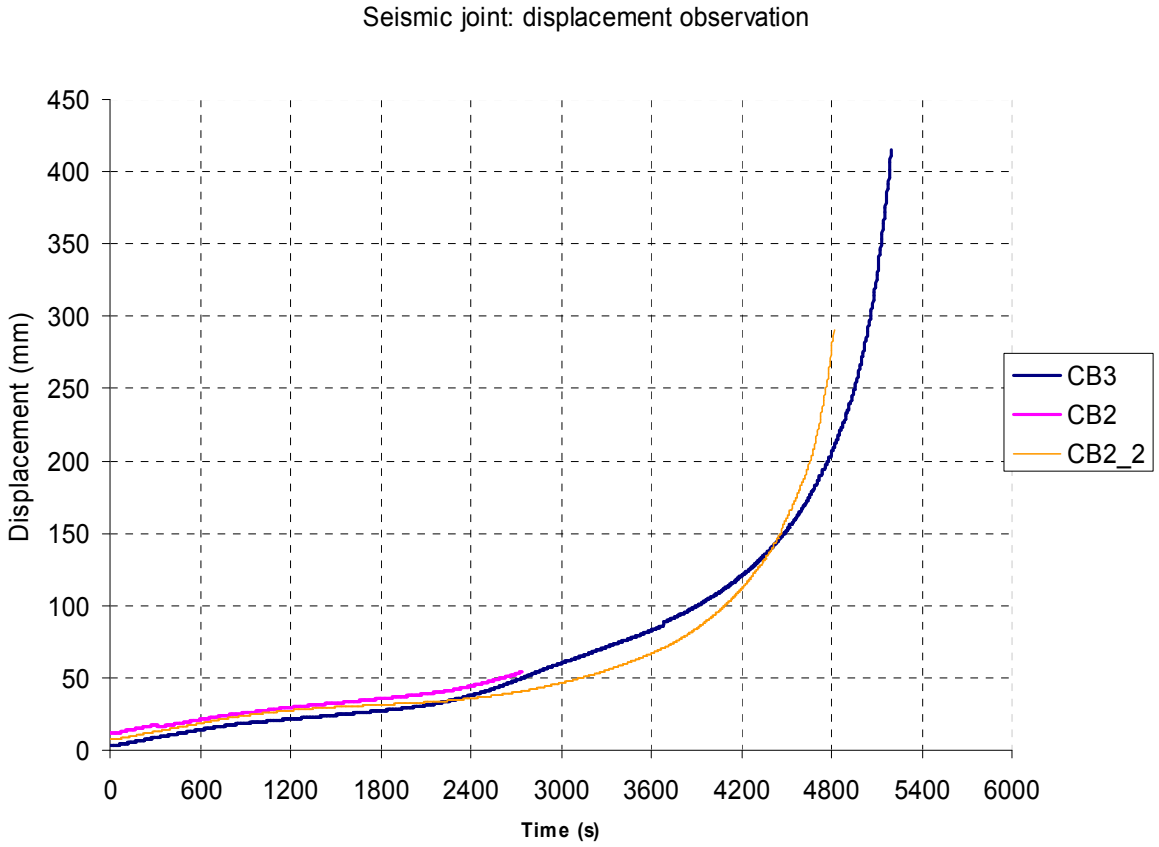

Figure 56. Total displacement given by tests (similar for CB2 and CB3)

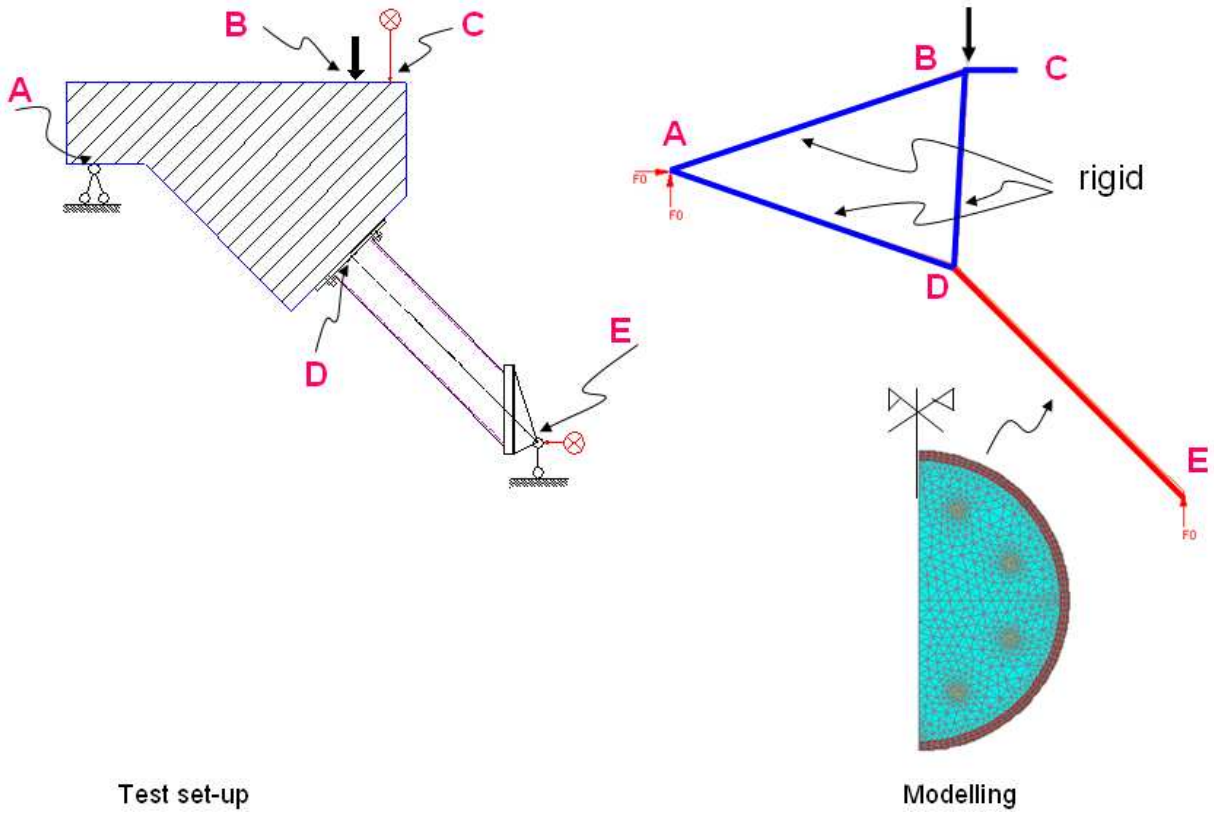

Figure 57. Mechanical modelling of the tests on CB2 and CB3 (using beam elements)

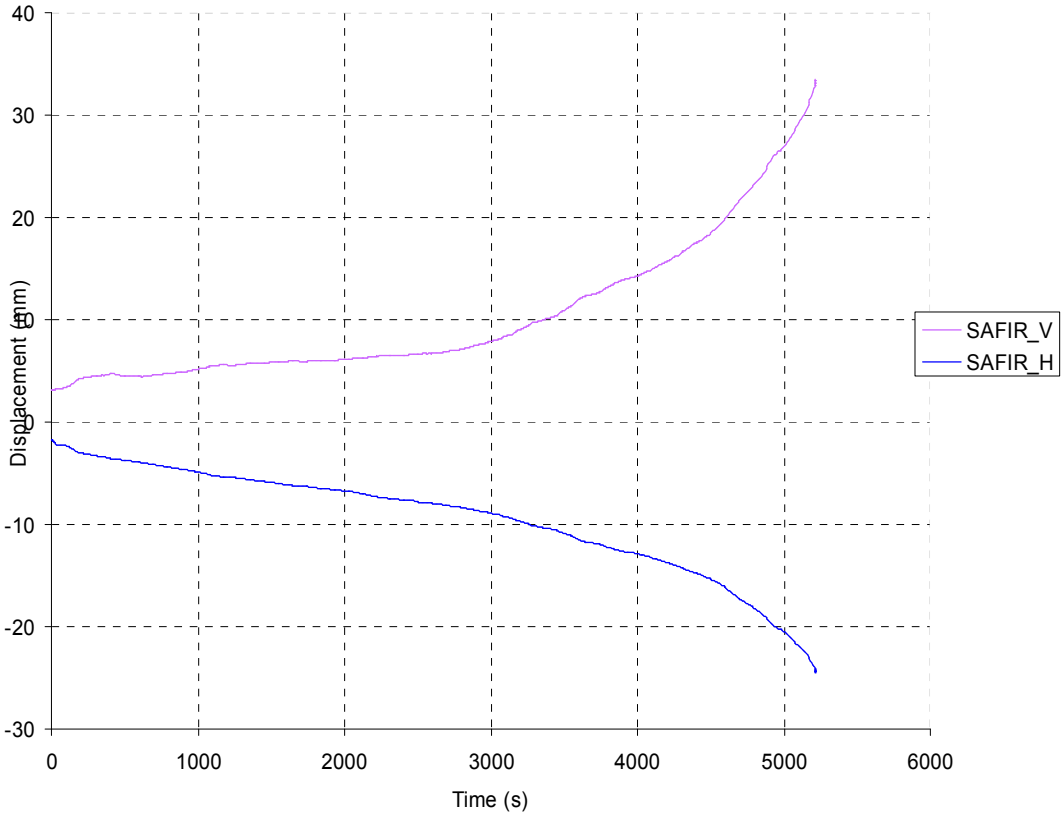

Figure 58. Displacements given by SAFIR

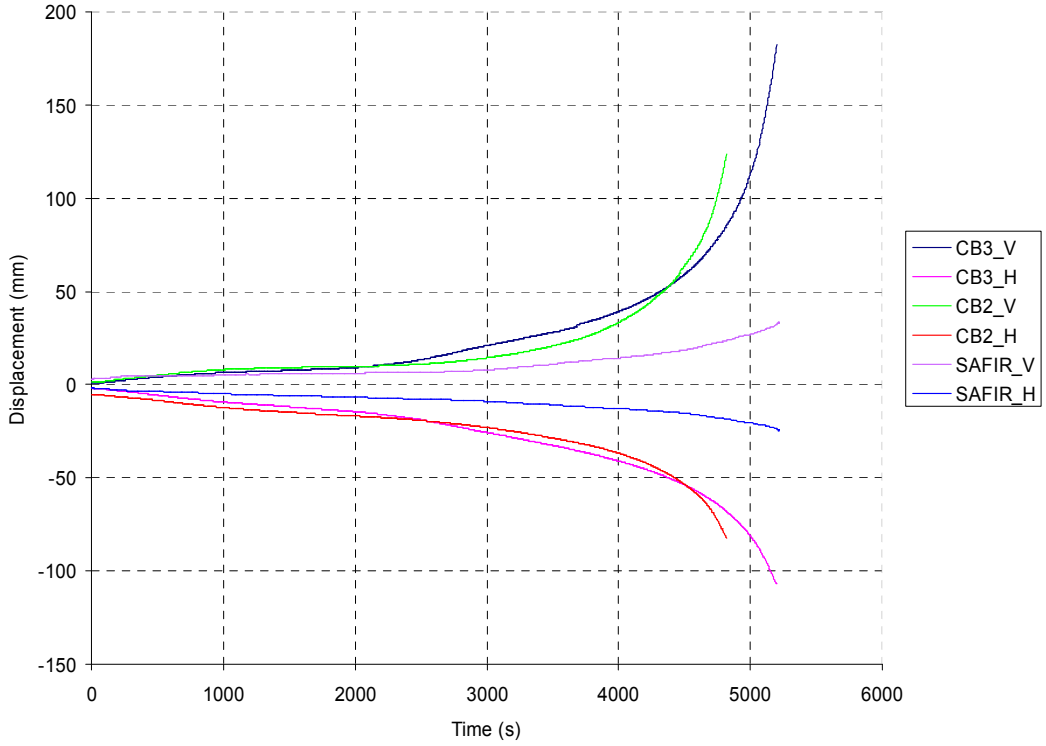

Figure 59. CB2 and CB3 - comparison of displacements

Concluding remarks

From the numerical results, the following remarks can be drawn for the moment:

- The 2D model can be used to calculate the temperature development in the rebars of the slap and in the vertical plate of the static joints while 3D model is recommended for the other components. The parametric study on the temperature developments are needed such that the simple guidelines can be given, this is a future perspective of the work.
- The beam elements can be used in the mechanical analysis for seismic joints and seismic column bases. In the seismic joints, the beam sections should be varied according to the actual configuration of joints. With respect to the column base, the influences of the end plate, the bolts and the stiffeners to the fire resistances may be neglected, the fire resistance of the column bases may be considered as the composite column one.

D.5.2.5. Numerical analysis for vertical plate of static joints

This section presents the numerical study on the "vertical plate" component of the static joints. The static joints were tested in fire condition within WP4 while four (3) "vertical plate" components were tested at the normal temperature in WP3.

Notices **(**Figure 60**)**

t: thickness of the plate;

h: height of the plate;

b: width of the plate part outside the tube;

D: inside diameter of the tube;

F_{Ed}: design value of the horizontal component of the load;

V_{Ed}: design value of the vertical component of the load;

α: load direction;

E: Young modulus;

υ: Poisson ratio.

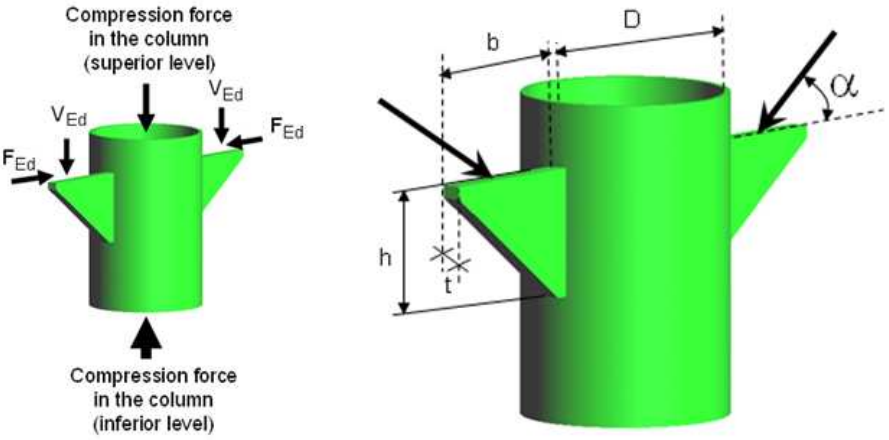

Figure 60. Beam-to-column joints - through plate component

General considerations and hypotheses

Figure 61 describes the buckling mode of the whole joint while the buckling mode of the through plate is shown on Figure 62.

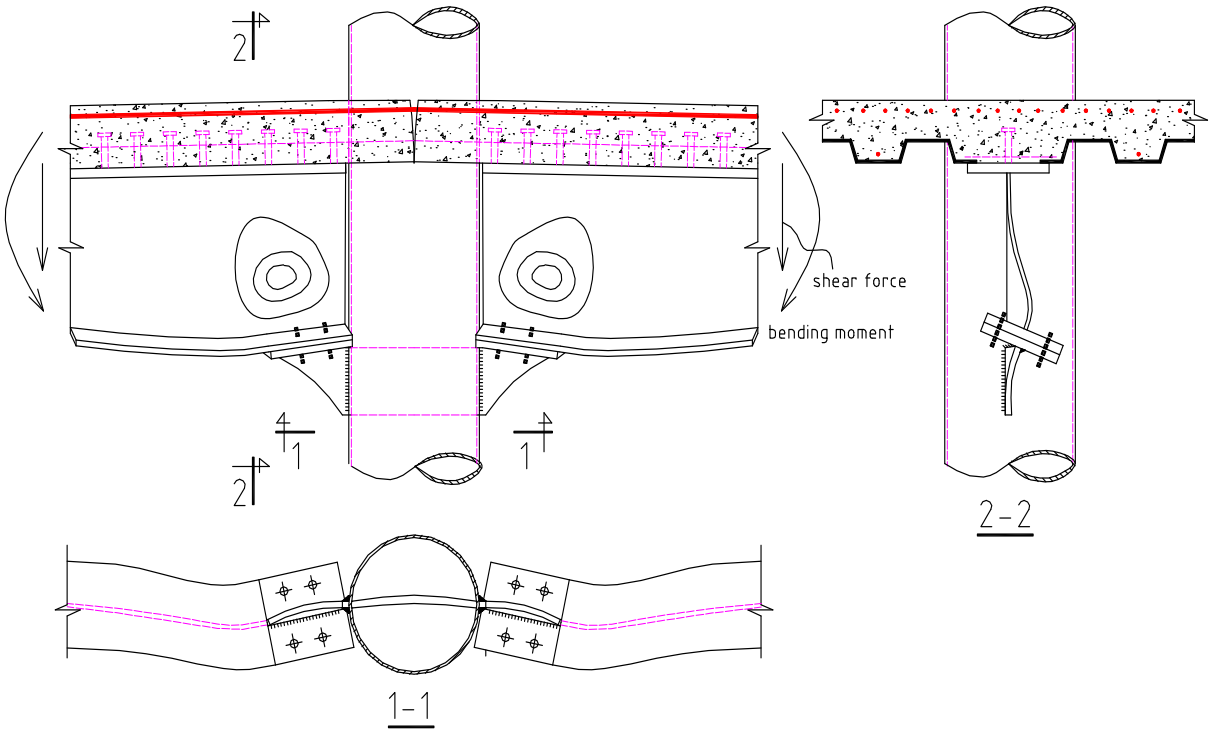

Figure 61. Buckling mode of joint

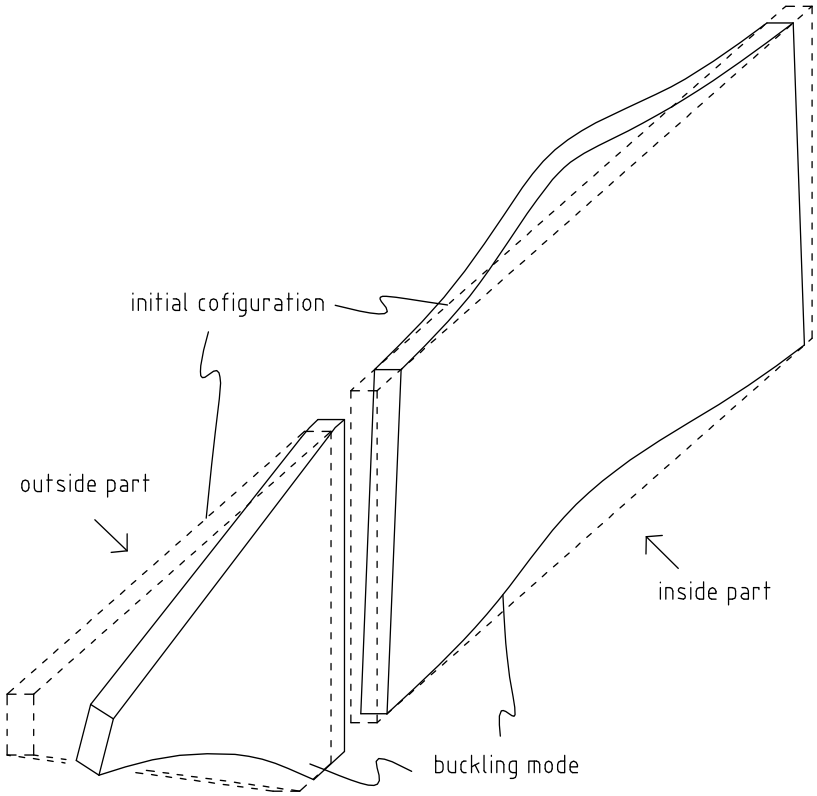

Figure 62. Buckling mode of through plate

For the simplification reason, the through plate is devised into two parts, inside part (inside the column) and outside parts (outside the column) with the boundary and loading condition as the show on Figure 63. The buckling theory of plate is applied to study the strength of each part.

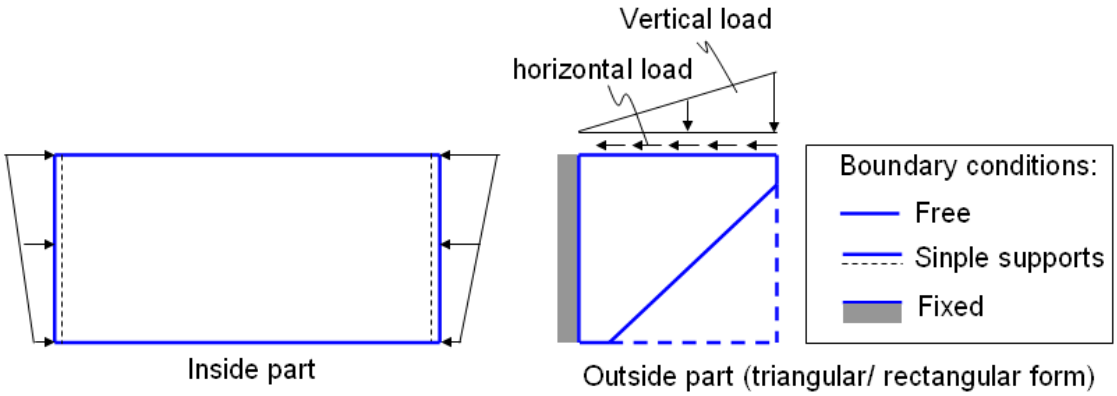

Figure 63. Modelling of boundary and loading for the through plate

Using the buckling theory of plates, the buckling stresses of the inside and outside parts can be written by the following equations:

$$\sigma_{c,ou} = \mu_1 \frac{\pi^2 E}{12(1-\nu^2)}\left(\frac{t}{b}\right)^2;$$

$$\sigma_{c,in} = \mu_2 \frac{\pi^2 E}{12(1-\nu^2)}\left(\frac{t}{h}\right)^2.$$

Numerical investigation

The coefficients μ_1 and μ_1 in above equations are used to take into account boundary condition, loading condition, plasticity and initial imperfection. In this work, these coefficients are determined by the numerical analysis, as:

$$\mu_1 = (\sigma_{c,ou})_{numerical} \Big/ \left(\frac{\pi^2 E}{12(1-\nu^2)}\left(\frac{t}{b}\right)^2\right); \qquad \text{(D.5.2.5.1)}$$

$$\mu_2 = (\sigma_{c,in})_{numerical} \Big/ \left(\frac{\pi^2 E}{12(1-\nu^2)}\left(\frac{t}{h}\right)^2\right), \qquad \text{(D.5.2.5.2)}$$

with $\sigma_{numerical}$ is calculated by LAGAMINE (a nonlinear finite element code developed in University of Liege) considering the boundary condition, the loading, the plasticity and the initial imperfection, as the description on Figure 64 and Figure 65. In the numerical models, 3D solid elements are used.

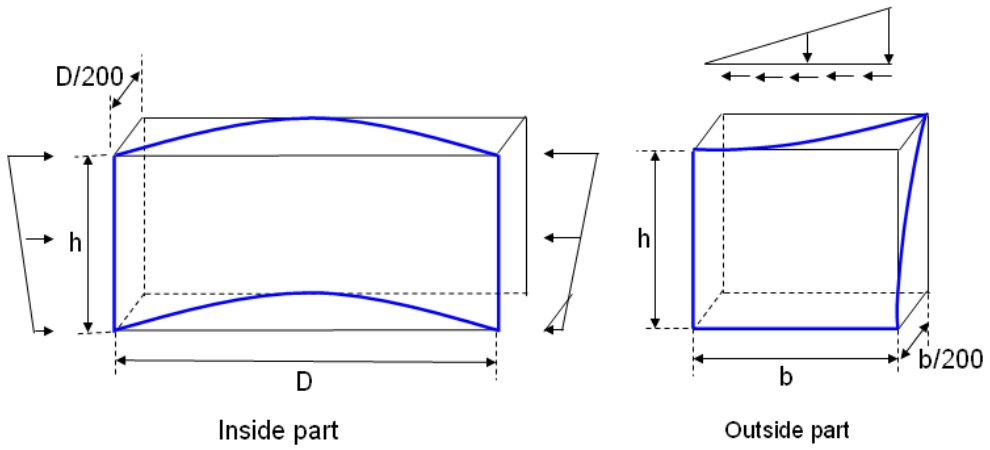

Figure 64. Modeling of the initial imperfection for the plate

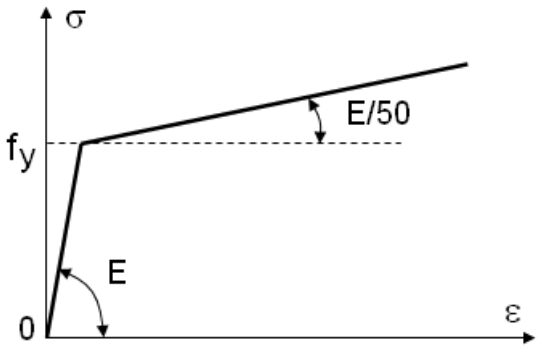

Figure 65. Material modelling in the numerical analysis

In order to validate the FE model, some examples existing in the literature [14] are examined, as the following.

Problem 1: simple supported, square plate under uniaxial load [14]. Elastic modulus E=10,700 ksi, yield strength σ_0=61.4 ksi. In [14], Ramberg-Osgood material $\varepsilon = \sigma / E + k\sigma_0 / E(\sigma_0 / E)^c$ with c=20 and k=0.3485 is applied while the material described in Figure 65 is adopted in LAGAMINE. The initial imperfection 1/200 as the recommendation of Eurocode 3, part 1-5 (on plated structures) is adopted (Figure 66). The comparison of the results is presented in

Table 18 18. The buckling stress given by LAGAMINE is closed with the Bleich's one.

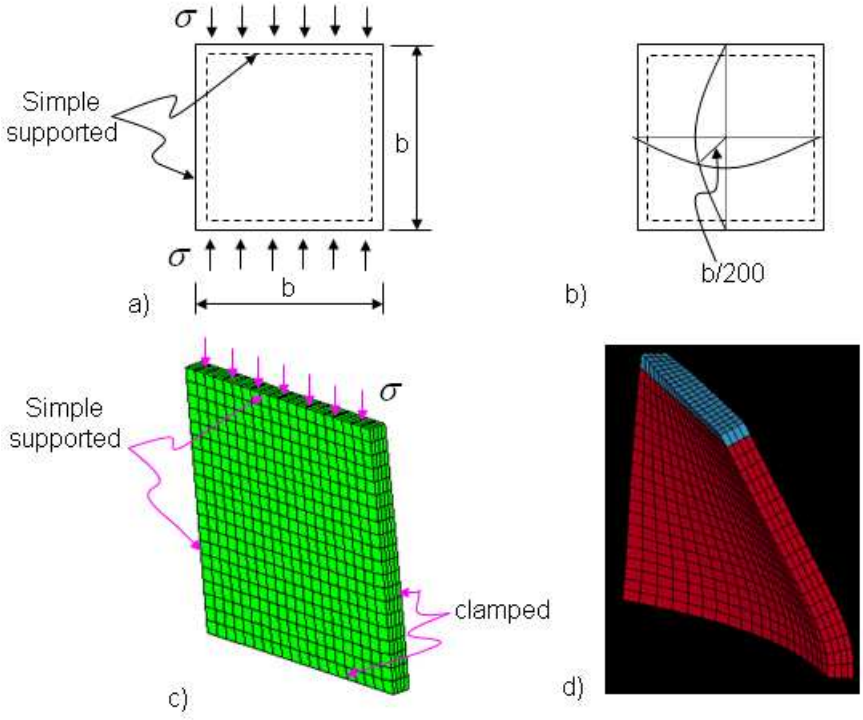

Figure 66. Problem 1: a) plate outline b) initial imperfection used in LAGAMINE; c) FE modelling in LAGAMINE; d) Buckling mode given by LAGAMINE

Table 18. Problem 1 - Comparison of results

b/t	Buckling stress (in ksi)			
	IT	DT	Bliech's theory	LAGAMINE
22	70.844	60.080	56.125	51.460
23	65.166	58.836	55.139	50.366
24	60.713	57.397	54.109	49.258
25	57.363	55.730	52.988	48.090
26	54.598	53.806	51.712	47.289
27	51.938	51.569	50.185	46.520
28	49.112	48.962	48.269	45.642

Problem 2: A quite thick plate is considered in this example. Free-Simple-Free-Simple square plate under uniaxial plate was studied by Wang et al (2001) [14] with the variation of thick/wide ratio and also the Ramberg-Osgood parameters are varied.

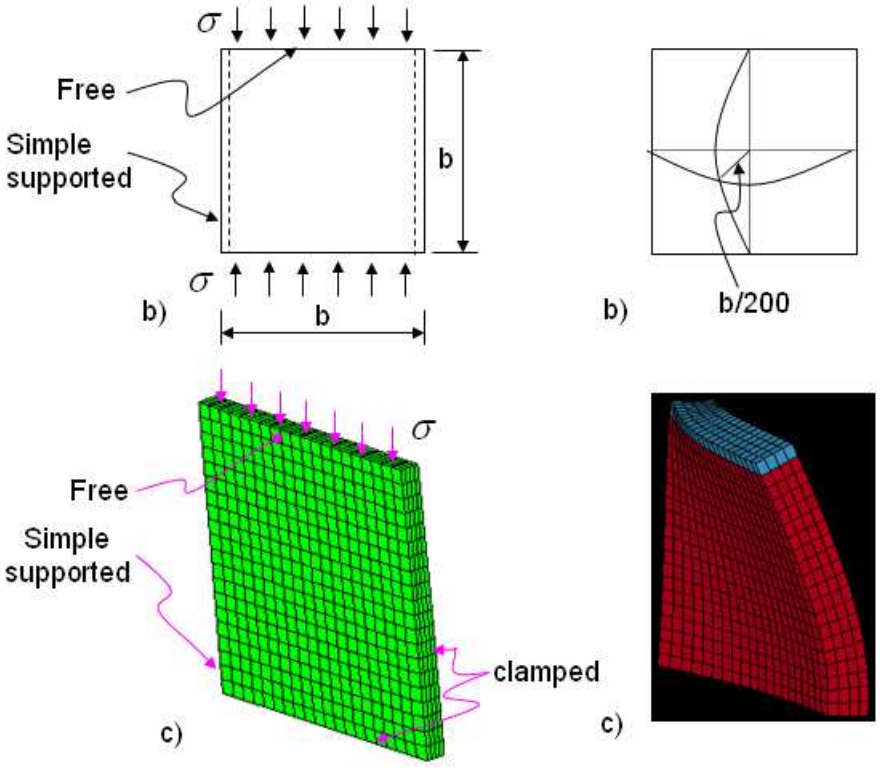

Figure 67. Problem 2: a) plate outline b) initial imperfection used in LAGAMINE; c) FE modelling in GAGAMINE; d) Buckling mode given by LAGAMINE

Table 19. Problem 1 - Comparison of results

Buckling stress factor $\sigma_c tb^2/(\pi^2 D)$			
E/ σ_0	IT	DT	LAGAMINE
200	1.136	0.999	0.966
300	1.104	0.819	0.686
500	1.104	0.473	0.434
750	1.104	0.298	0.215

The results given by LAGAMINE are closed with the DT one. It can say that in this case the buckling stress factors coming from IT are not reasonable because they don't change when yield strength varies.

The present model is used for the present case (vertical plate of static joints) with the modification of boundary conditions (Figure 63). The parametric study (the geometric dimensions of the plate are varied such that almost practical case can be coved) is performed, and the corresponding values of μ_1 and μ_1 are obtained (the detail values can be found in Deliverable 6).

D.5.2.6. Numerical analysis for "end plate" component of static column bases

One static column base was tested at normal temperature under cyclic loading in WP3, and one same configuration of the column base was also tested in fire condition within WP4. Moreover, three (3) "end plate" components were tested at normal temperature under monotonic loading in WP3. This section presents the numerical investigation for the "end plate" components. The details on the geometrical and mechanical properties of the investigated components can be found in Deliverable D3.

Numerical strategy

A finite element model has been developed, using a homemade finite element model called LAGAMINE able to reflect the full non-linear behaviour of elements subjected to large deformations, in order to simulate the behaviour of the joints. The main features of the proposed numerical model may be summarized as follows (Figure 68):

- 3D solid element are used;
- Agerskov's conception for the bolt shank length (see Agerskov (1976)) is adopted (Figure 69 and Table 20)
- Plastic nonlinear material is introduced with the natural curve that is established from nominal curve given by the coupon tests (see Deliverable 3).
- Geometrical nonlinearities (large deformation) are taken into account;
- Contact between the joint components (bolts-flanges, flange-flange) is modelled;
- Geometry of the weld is introduced (but the weld material is assumed to have the same properties as the tube steel);

- The bolts in the compression zone is not considered;
- The geometries of the investigated specimens are presented in
- Table **21**.

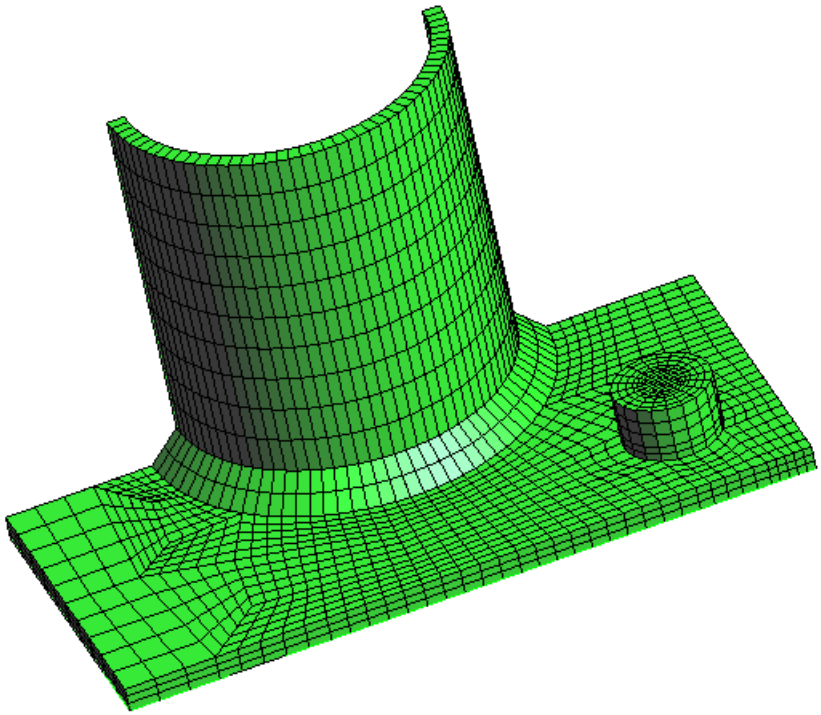

Figure 68. FE modelling for “end plate” component

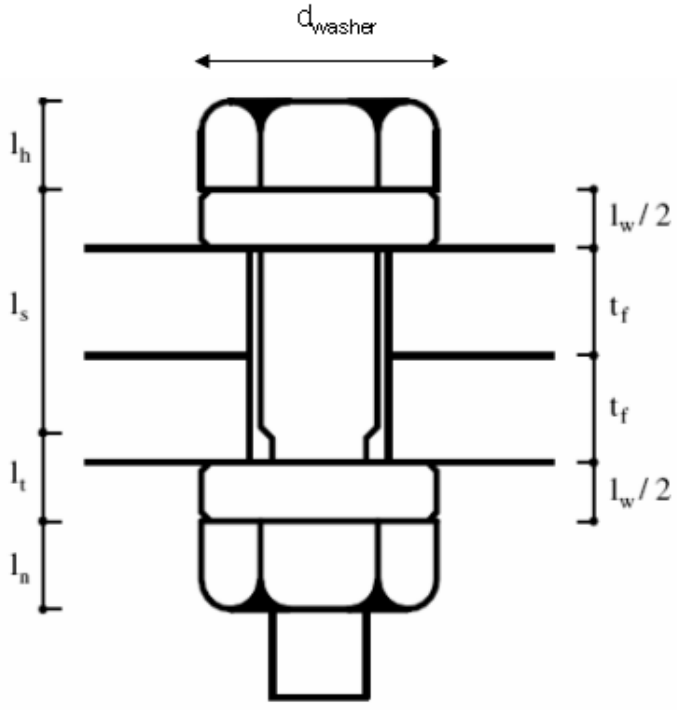

Figure 69. Geometries of the bolts

Table 20. Detail value of bolt geometries (Figure 69)

Bolts	A_b (mm^2)	A_s (mm^2)	t_f (mm)	l_h (mm)	l_n (mm)	l_s (mm)	l_t (mm)	l_w (mm)	d_w (mm)	l_{eff} (mm)
Specimen 1	707	566	14	18.5	23.7	41	5	18	56.5	65,1

Specimen 2	707	566	16	18.5	23.7	41	0	9	56.5	52,9
Specimen 3	707	566	18	18.5	23.7	41	4	9	56.5	57,5

Table 21. Geometries of the investigated specimens

Specimen	Geometries (mm)								Material strength (N/mm2)	
	b	h	t_p	d	e_1	e_2	w	a	f_y	f_u
1	400	400	14	193.7	60	60	23.685	16	418	602
2	400	400	16	193.7	60	60	23.685	16	418	602
3	400	400	18	193.7	60	60	23.685	16	418	602

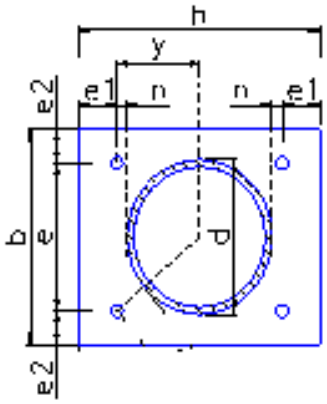

Results

The deformation and the load-displacement curves given by the numerical analysis are compared with the experimental one. The deformation is in good agreement (Figure 70) while the difference about 10% for the load-displacement curves (Figure 71 to Figure 73).

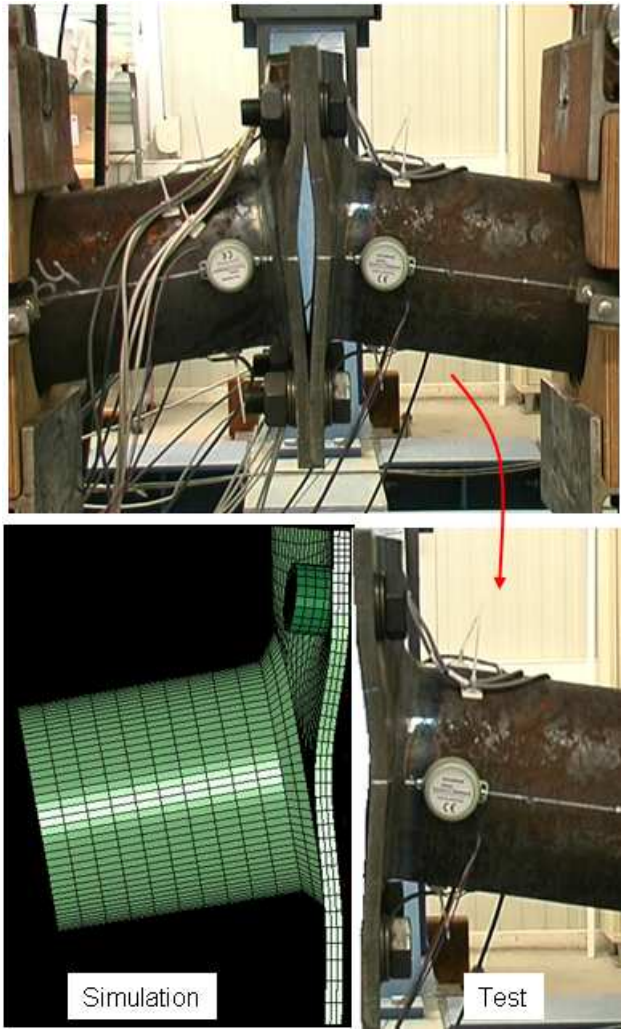

Figure 70. “End plate” component – comparison of deformation

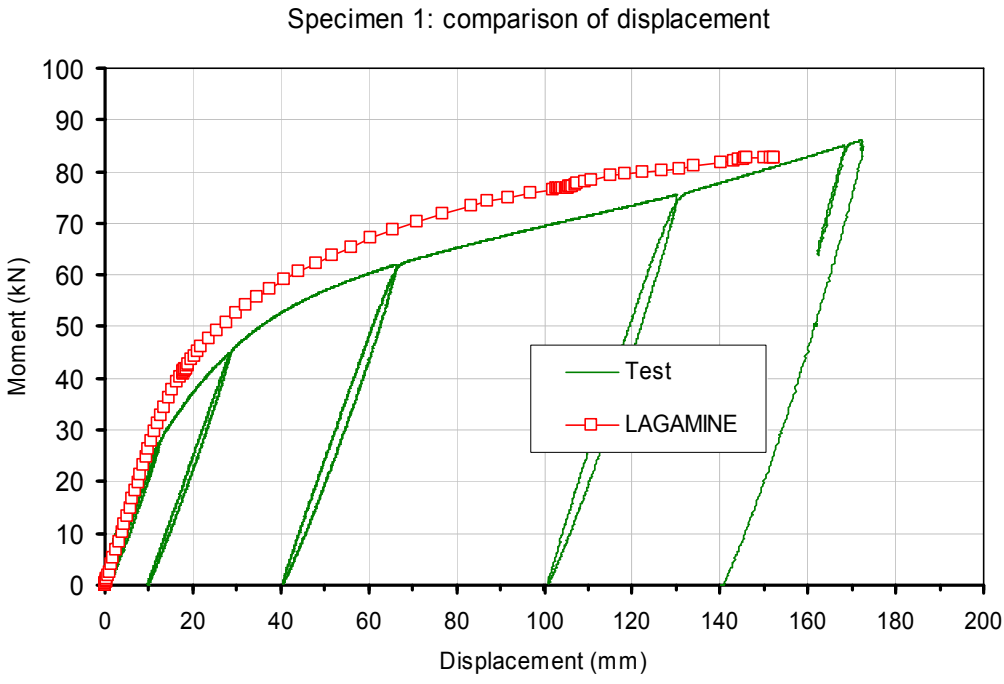

Figure 71. Sepecimen 1– comparison of load – displacement curves

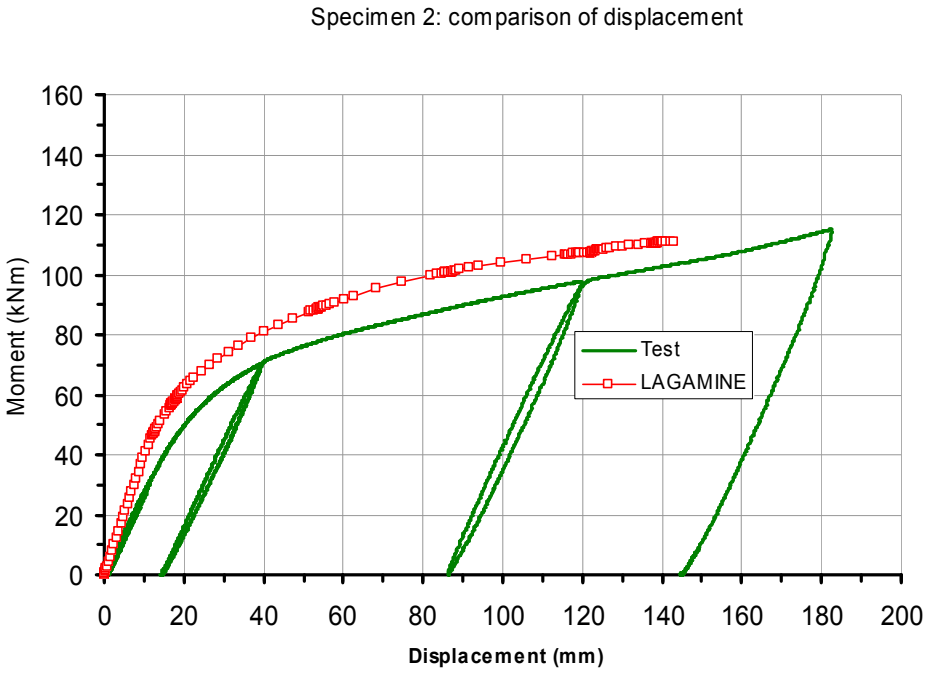

Figure 72. Sepecimen 2– comparison of load – displacement curves

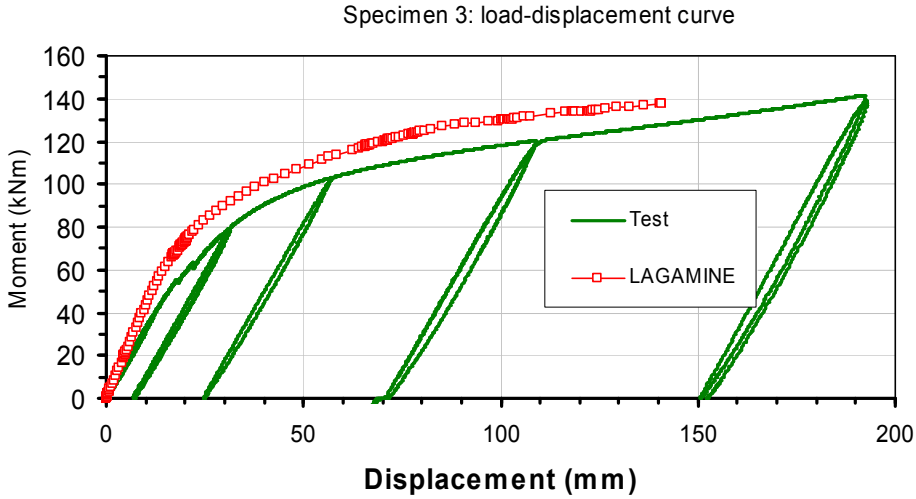

Figure 73. Sepecimen 3– comparison of load – displacement curves

D.5.3. Parametric numerical analysis

On the basis of the calibration of 2D-3D numerical models, parametric numerical analyses were conducted in order to investigate the response both of columns and of joints and of the prototype structure. The analysis took into account different input and/or different bond conditions in order to evaluate the effects on the response.

D.5.3.1. Analysis of the behaviour of columns at room temperature

Extensive numerical investigation is being conducted throughout the present project in order to develop stability curves and interaction diagrams, considering the influence of the initial imperfections to the ultimate beam-column capacity. The development of stability curves provided the opportunity to

investigate thoroughly the post-buckling behavior of imperfect HSS beam-columns as reported in the following sections. Towards this effort, basic parametric investigation has been conducted for the optimization of the finite element modeling tools.

D.5.3.1.1. Buckling response of axial loaded tubular members

In order to estimate the stability curves for high strength steel tubular members, the buckling behavior was investigated in terms of the member slenderness and the amplitude of the initial crookedness e_0. Load displacement curves were developed under axial compression for the HSS (TS590) imperfect (e_0=L/300) tubular member with D=355mm, t=8mm as shown in Figure 74.

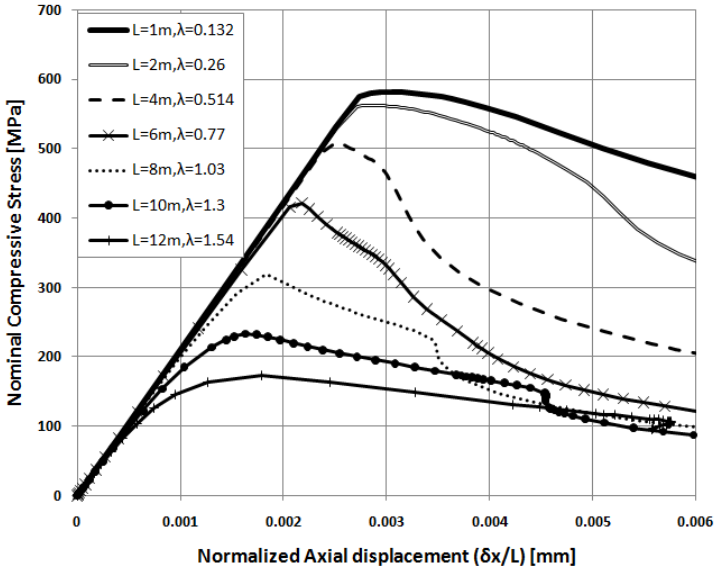

Figure 74. Comparison of load displacement paths for HSS tubular members with D=355mm, t=8mm (D/t=44) and different values of member slenderness.

It is shown that for a short relatively thin tube, buckling occurs progressively while plastic deformation is growing larger in the plastic region and the post buckling curve appears to be rather smooth. For intermediate values of member slenderness the transition from the elastic to the elastic-plastic region appears to be sharp and buckling occurs suddenly before the maximum capacity load is achieved. Additionally, it is shown that the buckling capacity load is significantly reduced when slender tubes are considered above the value of member slenderness λ=0.5.

Moreover, the deformation of the pipe wall for low and intermediate values of member slenderness is shown in Figure 75 and in Figure 76, respectively. More specifically, for short cylinders with D/t=44.375 (class 4), local buckling occurs far from the peak axial load and buckles are developed in a non-symmetric form perpendicular to the longitudinal direction of the tube at the tube mid span, while for intermediate values of member slenderness the non axi-symmetric buckles are developed in a symmetric form corresponding to the axis coinciding with the longitudinal direction of the tube.

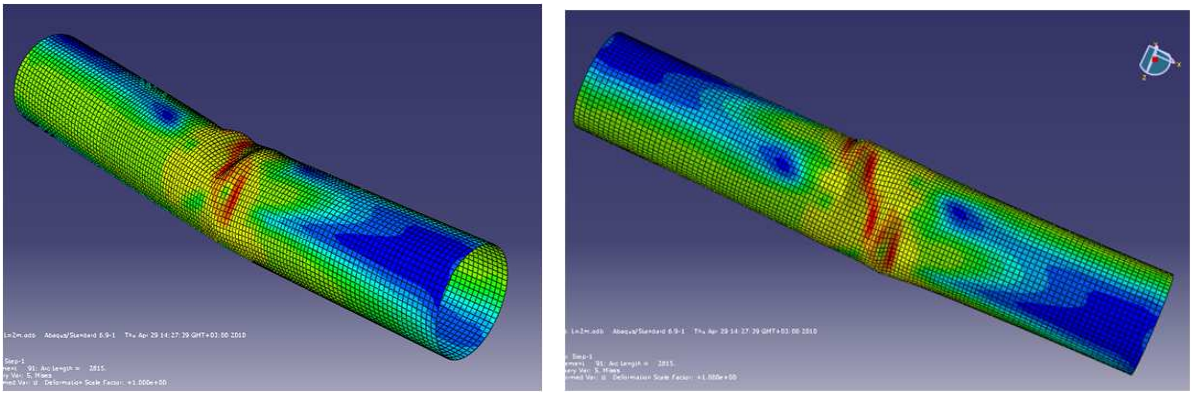

(a) *(b)*

Figure 75. (a) Failure mode due to shell buckling and (b) the final non-axisymmetric buckle development for the model with D/t=44.375 and L=2m (λ= 0.26)

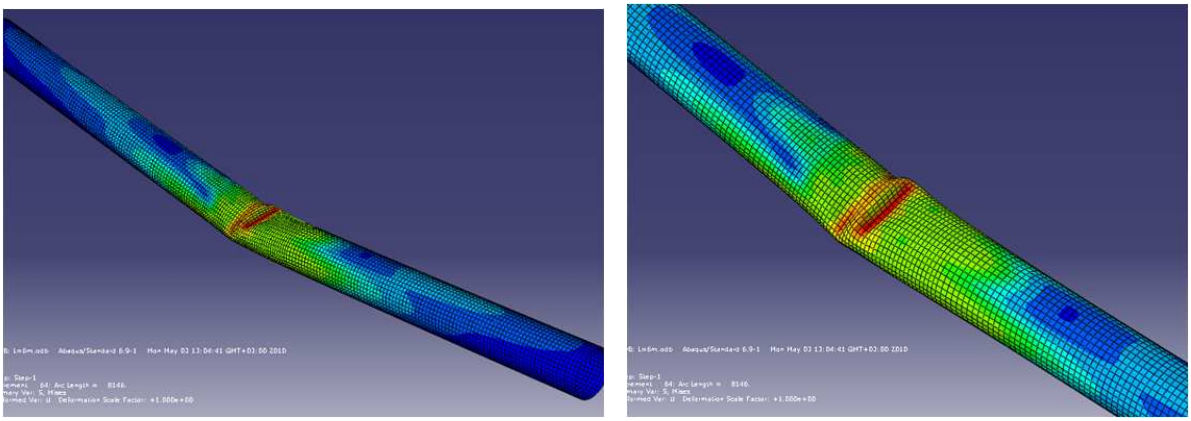

(a) *(b)*

Figure 76. (a) Failure mode due to a combination of global and local buckling and (b) non-axisymmetric buckle development for the model with D/t=44.375 and L=6m (λ=0.77)

Similarly, load-displacement paths and the buckle development on imperfect (e_0=L/300) HSS tubes with D=355mm, t=12mm under axial compression are developed as shown in Figure 77 and in Figure 78, respectively.

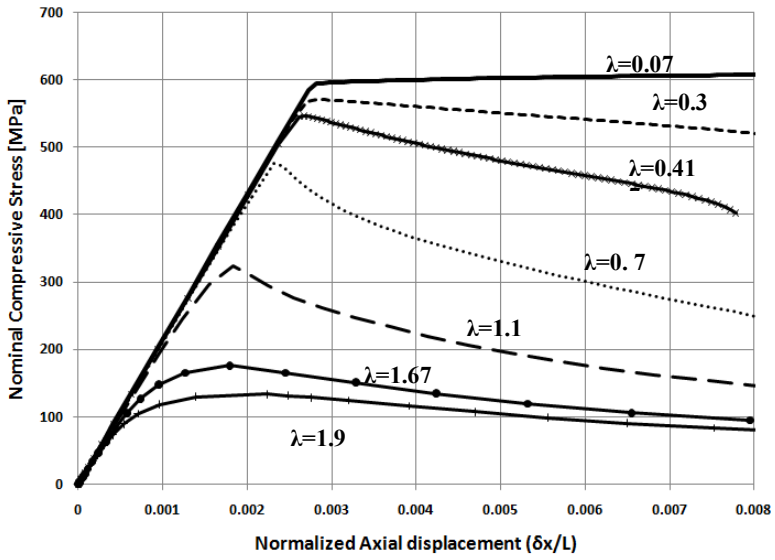

Figure 77. Comparison of load-displacement curves for tubular members with D=355mm, t=12mm (e_0=L/300) for different values of member slenderness

The above Figure indicates that the buckling capacity load is significantly reduced as member slenderness is increased (λ>0.5). For short tubular members, buckling occurs while material plastic deformation is gradually increased under plastic regime and the post buckling curve appears to be rather smooth. For intermediate values of member slenderness there is a sudden abrupt change in the slope of the load displacement curve. At this point, local buckling occurs before the maximum capacity load is achieved.
The deformation of the pipe wall for low and intermediate value of member slenderness is shown in Figure 78. As shown, for short cylinders with D/t=29.58 (class 4), buckles are developed in a non-symmetric form perpendicular to the longitudinal direction of the tube close to the capped ends due to the influence of the boundary conditions. For intermediate values of member slenderness a single smooth buckle is developed towards the inner part of the cross section perpendicular to the longitudinal direction.

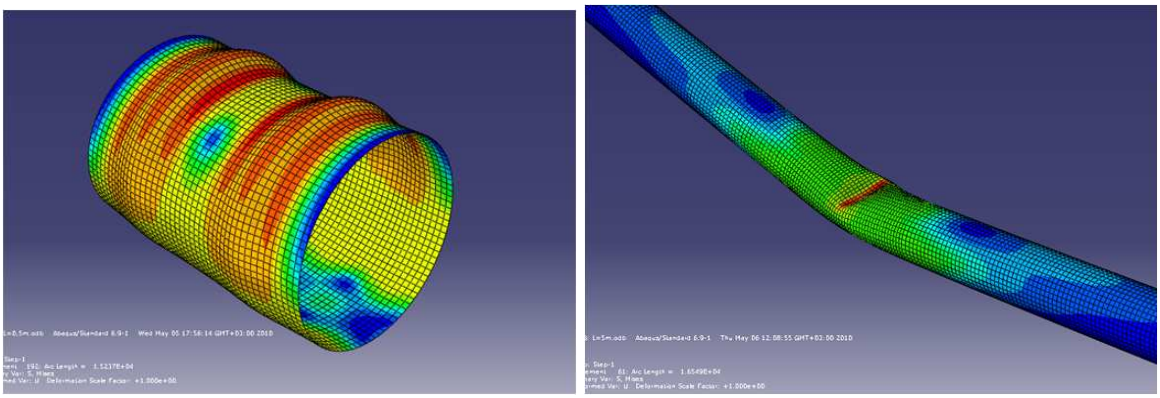

(a) (b)

Figure 78. The failure mode of the tube model with D/t=29.58 (a) due to shell buckling for the model L=0.5m (λ=0.07) and (b) global buckling of the tube with L=5m (λ=0.7)

In order to define the buckling strength sensitivity in the presence of initial imperfections and the corresponding post buckling behavior, load displacement curves of a model tube of D=355mm, t=12mm and L=3m with e_0=L/300 and e_0=L/500 are compared as shown in Figure 79. It is illustrated that the buckling strength considering e_0=L/500 is not significantly reduced (2%) compared with the case of e_0=L/300.

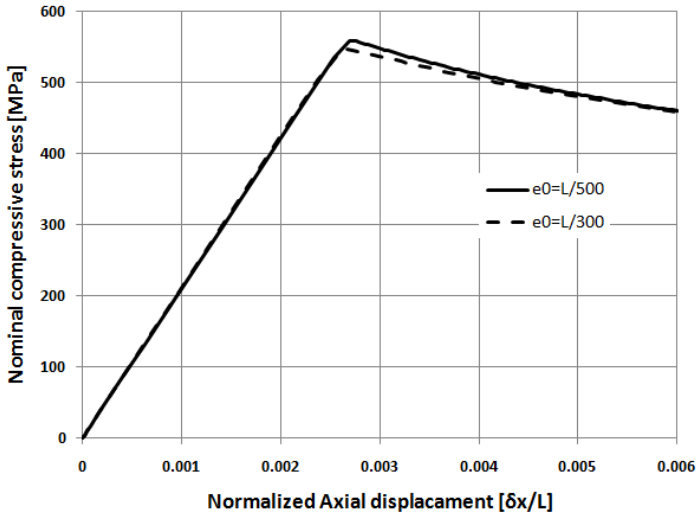

Figure 79. Comparison of load-displacement curves for HSS tubular members with D=355mm, t=12mm and L=3m for e_0=L/300 and e_0=L/500.

D.5.3.1.2. Analysis of the prototype structure under seismic loading

In order to evaluate the response of the structure under seismic loading the 2D moment resisting frame was analysed by time history analysis. As shown in Figure 80 two different frames were considered,

using both beam-to-column and base-column joints through the model obtained in the previous calibration. The difference between the aforementioned frames were column-base joints, i.e. the standard and the innovative solution, respectively.

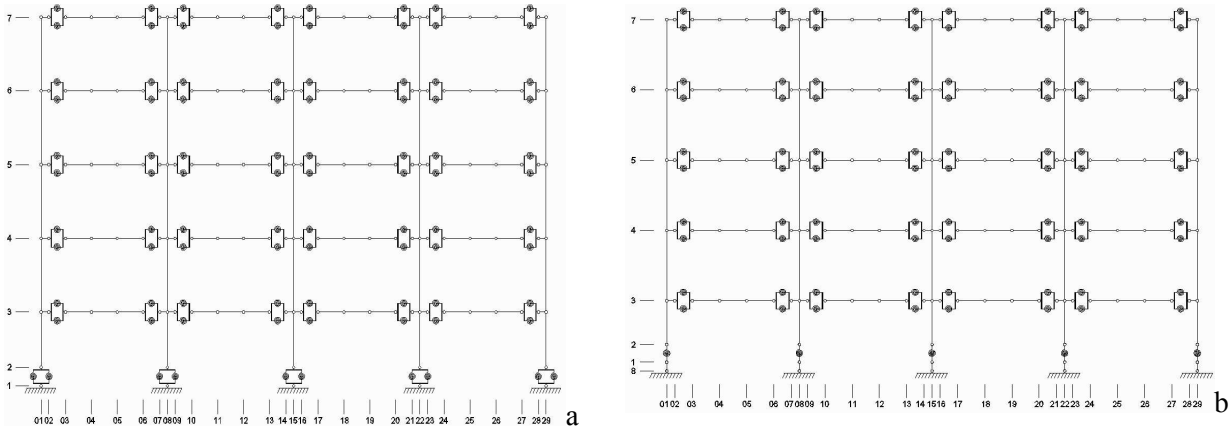

Figure 80. Modelling of 2D MRF: a) standard column-base joint; b) innovative column-base joint

The analyses were conducted using as input 3 artificial accelerograms matching the elastic response spectra in agreement with EN1998 Part 1 (2005); Figure 81shows one of the accelerograms used

To evaluate the response and to estimate the q factor as shown in Figure 82 [4], the following parameters were considered: i) the interstorey drift; ii) the response of joints in term of stiffness and strength degradation; iii) different levels of peak ground acceleration.

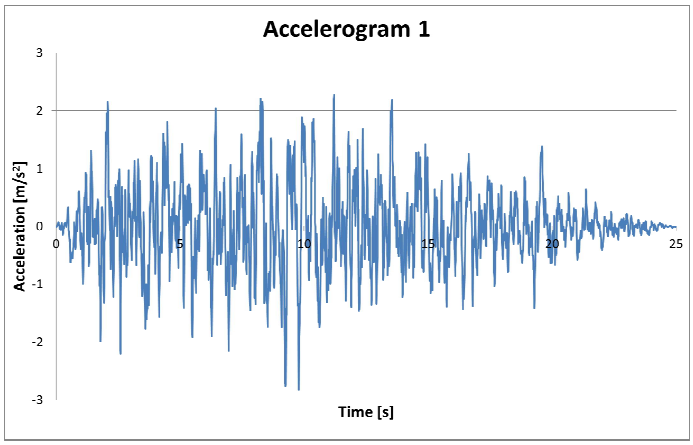

Figure 81. Artificial accelerogram matching the elastic response spectra

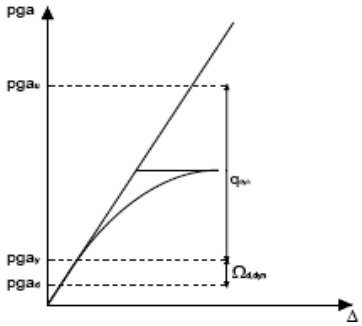

Figure 82. Behaviour and overstrength

With regard to the 2D Moment resisting frame with standard column-base joints, the moment-rotation relationships and respective acceleration values are shown in the following figures . In detail, Figure 84 shows the moment-rotation relationship, the joint and the value of acceleration associated with the yielding condition; while Figure 85 shows moment-rotation relationships, the joint and the value of acceleration associated with the ultimate condition for beam-to column joint and column-base joint, respectively.

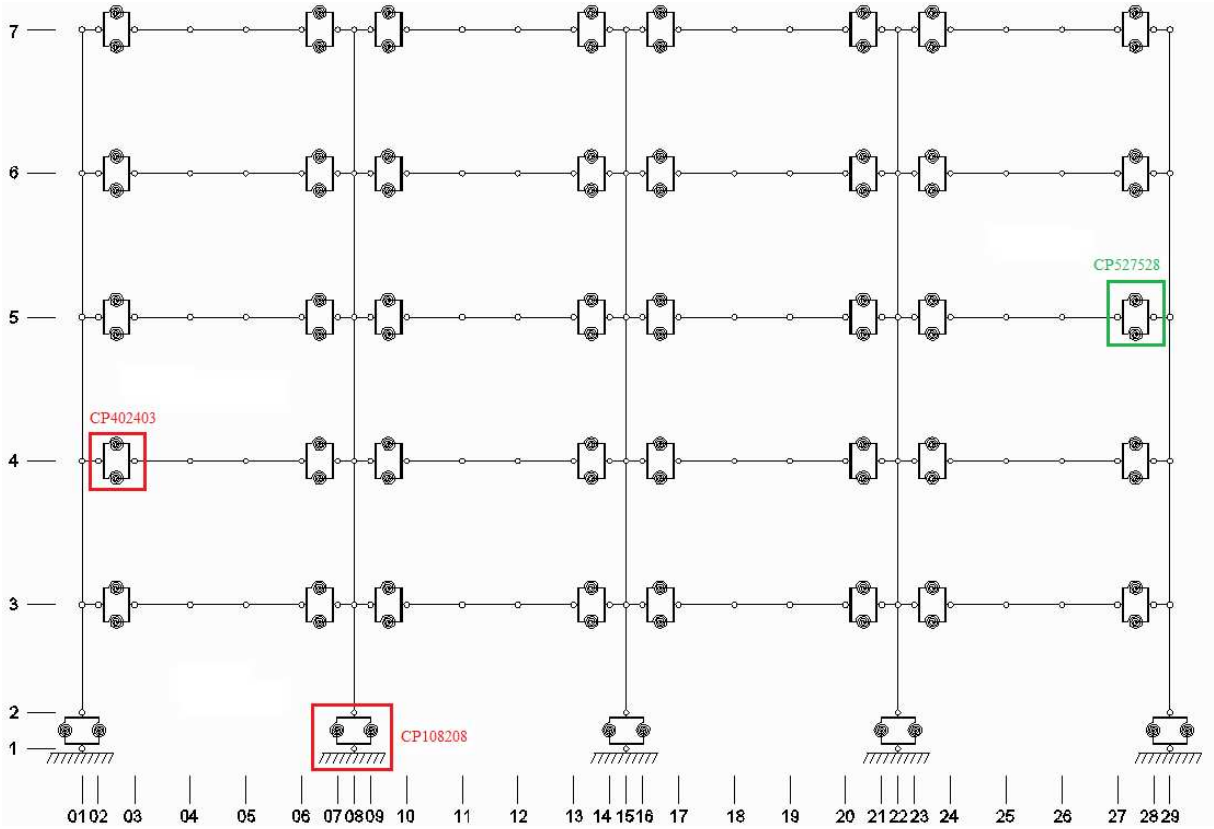

Figure 83. Position of significant plastic hinges obtained by non-linear numerical analysis

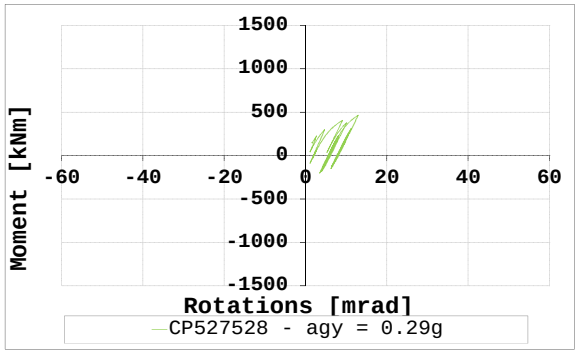

Figure 84. Moment-rotation relationship of the first joint yielded

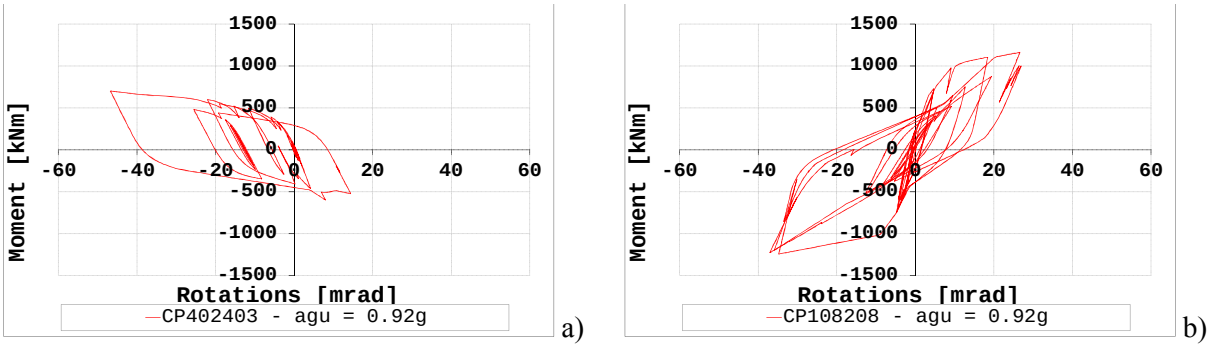

Figure 85. Moment-rotation relationship associated with final condition: a) beam-to-column joint; b) column-base joint

As a result, both joints and structures belong to the medium ductility class, characterized by: i) a plastic rotation of beam-to-column joints higher than 25mrad and with stiffness and strength degradation less than 20%; ii) a limited Interstory Drift (ID) of about 5% at failure; iii) a plastic rotation of both column-base joints considered higher than 41 mrad, in agreement with the request of ductility; iv) a q factor

estimated higher than the 3.2 value considered in the relevant design. Table 22 summarizes relevant results.

Table 22. Response parameters of the 2D moment resisting frames of Figure 80 under seismic loading

	With standard base-column joints			With innovative base-column joints		
Accelerogram	**1**	**2**	**3**	**1**	**2**	**3**
ag_y (g)	0.29	0.16	0.26	0.25	0.15	0.25
ag_u(g)	0.92	0.60	0.84	0.95	0.84	1.00
ID (%)	5.68	4.82	5.00	6.08	7.68	5.93
Q	3.23	3.87	3.23	3.86	5.57	4.00
Ω_{dyn}	3.38	1.84	3.08	2.90	1.78	2.96

D.5.3.2. Parametric study for the vertical plate of static joints

The numerical model proposed in Section D.5.2.5. is used in the parametric study with the variation of the plate geometries (Figure 60), and the corresponding values of μ_1 and μ_2 in Eqs. D.5.2.5.1 and D.5.2.5.2 are given for the practical design (See Deliverable D6).

D.5.3.3. Parametric study for the end plate of static column bases

An analytical model is also developed for the "end plate" component of static column bases (see Deliverable D6). The agreement between the analytical, numerical and experimental results is shown allowing parametric study by using the analytical. The detail on this parametric study is presented in Deliverable 6.

Appendix A: Material properties used in analysis of structures in fire

The available material law in SAFIR for the steel and the concrete are used with the following parameters.

A1. *Mechanic properties (at 20^0 C)*: the following values are given from the coupon tests within WP3 and WP4 (see Deliverable D3 and Deliverable D4).

- 324x10 Steel tubes (HSS): STEELEC3 with E = $2{,}1 \times 10^{11}$ N/m^2; $\mu = 0{,}3$; $f_y = 7{,}3 \times 10^8$ N/m^2.
- 356x12 Steel tubes (HSS): STEELEC3 with E = $2{,}1 \times 10^{11}$ N/m^2; $\mu = 0{,}3$; $f_y = 7{,}4 \times 10^8$ N/m^2.
- Rebar (S500): STEELEC2 with E = $2{,}0 \times 10^{11}$ N/m^2; $\mu = 0{,}3$; $f_y = 5{,}50 \times 10^8$ N/m^2.
- Concrete (C25/30): SILCONC_EN with $\mu = 0{,}3$; $f_c = 5{,}5 \times 10^7$ N/m^2; $f_t = 0{,}0$ N/m^2

A2. *Thermal properties*:

- Steel tubes (HSS) and Rebar (S500): STEELEC3 and STEELEC2 with

  Convection coefficient on hot surfaces: 25 W/m^{2}K

  Convection coefficient on cold surfaces: 9 W/m^{2}K

  Relative emissivity: 0,7

- Concrete (C25/30): SILCONC_EN with

  Specific mass: 2400 kG/m^3

  Water content: depends on each specimen, see Deliverable D4.

  Convection coefficient on hot surfaces: 25 W/m^{2}K

  Convection coefficient on cold surfaces: 9 W/m^{2}K

  Relative emissivity: 0,56

  Parameter for thermal conductivity: 0,5

References

[1] Agreskov H (1976). High strength bolted connections subject to prying. J. Struc Div.

[2] AISC-LRFD (2000). Load Resistance Factor Design Specification for steel hollow structural sections. American Institute of Steel Construction, Chicago, Illinois.

[3] American Petroleum Institute (1993). Recommended Practice, Designing and Constructing Fixed Offshore Platforms-Load and Resistance Factor Design. Recommended practice 2A-LRFD, 1st Edition. Washington.

[4] Bursi O. S., Zandonini R., Salvatore W., Caramelli S., and Haller M. (2006). "Seismic Behavior of a 3D Full-Scale Steel-Concrete Composite Moment Resisting Frame Structure", Composite Construction in Steel and Concrete V, 641 - 652. Proceedings of the 5th International Conference,ASCE,.

[5] Chen J., Young B. (2008). Design of high strength steel columns at elevated temperatures. Journal of Constructional Steel Research Engineering, 64:689-703.

[6] CIDECT (1992). Structural Stability with Hollow Sections. CIDECT design guide No. 2, Springer-Verlag.

[7] EN 1993-1-6 (2007). "Eurocode 3: Design of steel structures. Part 1-6: Strength and Stability of Shell Structures", CEN, Bruxelles.

[8] EN1992-1-1 (2005). "Eurocode 3: Design of concrete structures - Part 1-1: General rules and rules for buildings", CEN, Bruxelles.

[9] EN1993-1-1 (2005). "Eurocode 3: Design of steel structures - Part 1-1: General rules and rules for buildings", CEN, Bruxelles.

[10] EN1993-1-12 (2007). "Eurocode 3: Design of steel structures - Part 1-12: Additional rule for te extension of EN 1993 up to steel grades S700", CEN, Bruxelles

[11] EN1993-1-2 (2005). "Eurocode 3: Design of steel structures - Part 1-2: General rules - Structural fire design", CEN, Bruxelles.

[12] EN1998-1 (2005). "Eurocode 4: Design of structures for earthquake resistance - Part 1-1: General rules and rules, seimic actions and rule for buildings ", CEN, Bruxelles.

[13] Franssen J.M. (2005). SAFIR. A Thermal/Structural Program Modelling Structures under Fire, Engineering Journal, A.I.S.C., 42(3), 143-158.

[14] Wang C.M. et al (2001). Elastic/plastic buckling of thick plates. International Journal of Solid and Structures 38 (2001) 8617-8640.